School of Mechanical and Manufacturing Engineering

Faculty of Engineering

UNSW Sydney

BY

Maximilian Keller

A Review of Automotive Energy Harvesting Shock Absorber Technology, as Applied to a Case Study of the UNSW Sunswift VII Solar Vehicle.

Thesis submitted as a requirement for the degree of Bachelor in Mechatronic Engineering

Submitted: 23/04/23 Student zID: z5265207
Supervisor: Dr. Zoran Vulovic (UNSW)

ORIGINALITY STATEMENT

'I hereby declare that this submission is my own work and to the best of my knowledge it contains no materials previously published or written by another person, or substantial proportions of material which have been accepted for the award of any other degree or diploma at UNSW or any other educational institution, except where due acknowledgement is made in the thesis. Any contribution made to the research by others, with whom I have worked at UNSW or elsewhere, is explicitly acknowledged in the thesis. I also declare that the intellectual content of this thesis is the product of my own work, except to the extent that assistance from others in the project's design and conception or in style, presentation and linguistic expression is acknowledged.'

Signed 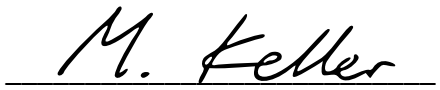

Date 23/03/23

Abstract

This report examines the feasibility of Energy Harvesting Shock Absorbers (EHSA) to replace the traditional viscous fluid dampers used in the suspension of vehicles. The literature review provides a critical evaluation of existing literature and commercial research involving Energy Harvesting Shock Absorbers for automotive applications. A comprehensive seven DOF full-car model was constructed to reflect the dynamics of the vehicle. Realistic road profiles could be generated based on the ISO 8608 standard. Furthermore, constraint criteria relating to the passenger comfort, road handling performance of the vehicle and physical suspension limitations were incorporated in the model. The simulation results were comparable to real-world experimental studies and revealed that the implementation of EHSA on the Sunswift VII solar vehicle could be worthwhile of pursuit.

Table of Contents

List of figures

List of tables

Nomenclature

English Symbols

a_{wz}	ISO 2631 frequency weighted vertical acceleration
c	Suspension damping constant
f	Time frequency
I_θ, I_ϕ	Pitch and roll inertia of the vehicle chassis
$K_{T,F}, K_{T,R}$	Front rear tyre stiffness
$K_{FL}, K_{FR}, K_{RL}, K_{RR}$	Front left, front right, rear left and rear right suspension stiffness
L_L, L_R, L_F, L_B	Distance of the centre-of-gravity to: left wheels, right wheels, front wheels, rear wheels
n	Spatial frequency
m_s	Sprung mass
m_u	Unsprung mass
$M_{FL}, M_{FR}, M_{RL}, M_{RR}$	Front left, front right, rear left and rear right wheel mass (unsprung masses)
M_B	Mass of the vehicle chassis
P	Power
u	Vehicle velocity
v_d	Suspension deflection velocity
W_k	ISO 2631 frequency weight
z_s	Sprung mass displacement
z_u	Unsprung mass displacement

Greek Symbols

ξ	Road handling performance index
ω	Angular frequency

Abbreviations

AC	Alternating Current
CAD	Computer Aided Design
DC	Direct Current
DOF	Degree of Freedom
eROT	Electromechanical Rotary (Suspension System by Audi)
EHSA	Energy Harvesting Shock Absorber
EMF	Electromotive Force
IRI	International Roughness Index
ISO	International Organisation of Standardisation
LTI	Linear Time Invariant

MEMS	Micro-Electromechanical System
MMR	Mechanical Motion Rectifier
PM	Permanent Magnet
PSD	Power Spectrum Density
PZT	Piezoelectric Transducer
QCM	Quarter Car Model
RMS	Root Mean Square
RTC	Real Time Clock
UNSW	University of New South Wales

1. Introduction

Shock absorbers used in vehicles and trucks are designed to damp out vibrations experienced due to the roughness of roads. In addition to comfort, suspension systems must provide good steering control and ensure the contact of the tyres with the road for predictable handling [10]. A conventional shock absorber reduces vibrations by means of viscous damping by converting the kinetic energy of vibrations into heat energy which is dissipated in a damper. Viscous dampers have been commonplace in the automotive industry for decades, however the constant drive for increased energy efficiency in vehicles has led to the emergence of innovative new research studies for energy recovery. In particular, the topic of regenerative suspension or Energy Harvesting Shock Absorbers (EHSAs) has caught recent research interest. Unlike conventional shock absorbers, which waste kinetic energy by dissipating it as heat, EHSAs aim to convert the vibration energy which is transmitted through vehicular suspension into electricity which can be stored and used in the vehicle.

The *UNSW* Sunswift VII Solar race car recently broke the world record for *the fastest electric vehicle on a single charge over the distance of 1000km*. In a drive to break further efficiency records and progress innovation in the electric vehicle sector, this report will focus on the *UNSW Sunswift VII Solar vehicle* as a case study, and asses the viability of introducing EHSA, to replace the existing dampers in the vehicle.

2. Literature Review

Energy Harvesting Shock Absorbers (EHA) can be categorised based on their operation principle in converting mechanical to electrical energy [11, 12]. Electrical energy can be created electromechanically through induction or through the charge created in piezoelectric materials resulting from induced pressure and latent heat [13]. A device which converts energy from one form to another can be referred to as a transducer [14].

2.1. Piezoelectric Transducer Based EHSA

Piezoelectric (PZT) transducers used in mechanical to energy to electrical energy conversion have on average three times higher energy density than electrostatic and electromechanical transducers [15]. PZT transducers have been thoroughly explored for micro-scale applications [16]. However, as explained by Mitcheson et al., the performance benefits of piezoelectric transducers are currently not scalable for larger applications and the superior energy density to electromagnetic transducers is lost as the generator size increase [11]. Additionally, PZT vibration harvesters only work efficiently at (high) resonant frequencies. Therefore, some studies discuss the feasibility of including a PZT generator in parallel to a conventional suspension system with the goal of preserving the damping performance of the conventional viscous damper, while generating some electrical energy [17, 18]. The resonant power output is found to depend on the vehicle unsprung to sprung mass ratio of the and suspension stiffness to tire stiffness ratio. The highest RMS harvested power found in existing literature of a PZT transducer combined with a conventional damper in a two DOF quarter car model simulation was only 1238 mW at resonance [18].

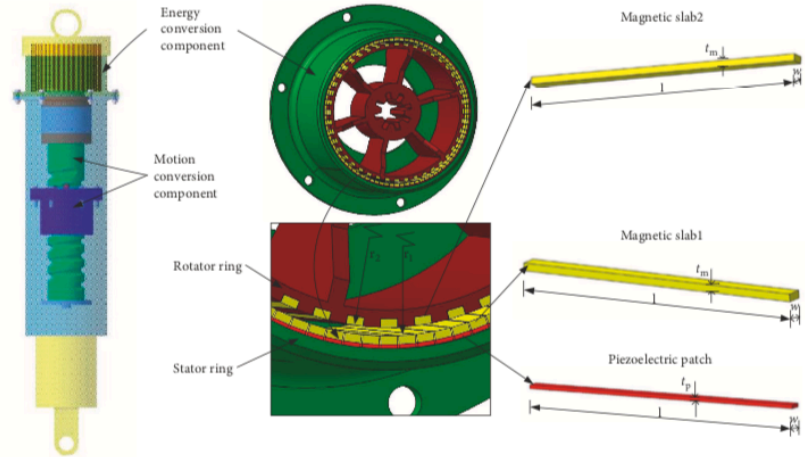

Figure 1: Geometry and schematic diagram of the rotational piezoelectric damper developed by [6].

In a recent study, Zhao, Wang et al. proposed one of the only real-life conceptual prototypes of a PZT based automotive shock absorber. It consists of a rotational magnet-based damper driven by a ball screw [6]. The EHSA which is illustrated in Figure 1, uses a radial array of magnetic slabs on a rotor and a second array of magnetic slabs on the stator surface. As the rotor rotates, a periodic magnetic repulsive

force acts between the stator and rotor which is transmitted to piezoelectric patches as shown in Figure 1. Although, 332.4W of power were generated during simulation, the simulation was based on an ISO 8608 grade D road profile and 1.5-tonne vehicle with speed of 120 km, which is unrealistic, as discussed in section 4.3 of this report. A more realistic estimate on ISO 8608 grade B – C road of the maximum attainable average power generation is ~20W [6]. Metrics on the damping force performance were not provided.

Currently, piezoelectric transducers are more suitable for microscale transducer systems such as microelectromechanical systems (MEMS) [19, 20]. Ergo, more studies are focussed on electromagnetic transducers, due to their better compatibility with automotive suspension.

2.2. Electromechanical Transducer Based EHSA

A distinction can be made between two categories of EHSAs in literature which employ electromechanical transducers in their designs. These categories are *direct drive* EHSA and *indirect drive* EHSAs [11]. Indirect EHSA make direct use of Brushed or Brushless DC electric motors to convert mechanical to electrical energy. Permanent magnetic DC motors can be directly used as generators, and will henceforth be referred to as a DC generators [21]. The most common form of generator used in literature regarding EHSA design and modelling are rare-earth permanent-magnet synchronous machines (PMSM) because they offer the highest torque-to-weight ratio among electric generators [22].

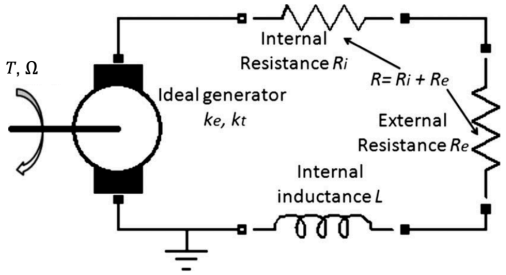

Figure 2: Electric circuit of a DC motor used as an electric generator, where R_e is the total resistance of the load; and R_i and R_e are the resistance and inductance of the generator coil.

The output torque T to angular speed Ω characteristic of permanent-magnet induction generators was experimentally investigated by [23] and analytically examined by [8, 24, 25]. The relationship is shown to linear until a ratio of angular velocity to pole frequency ω_p/p, where p is the number of pole pairs in the generator, is reached. The angular velocity ω_p represents an electromagnetic pole defined by

$$\omega_p = \frac{R}{L},$$

where R, is the total resistance of the rotor coil and external load, and L inductance of the rotor coils in the generator. The reason for the linear relationship until this point is due to eddy currents that are generated in the rotor as it rotates within this magnetic field of the stator. These eddy currents create their own magnetic field which opposes the original magnetic field, resulting in a braking force that is proportional to the speed of rotation. However, if the rotor speed approaches or exceeds the pole frequency, there are no longer any changes in magnetic flux and therefore no eddy currents are generated. As a result, the braking torque decreases and eventually becomes zero at synchronous speed, as shown by equation (1),

$$T = \frac{K_t K_e}{(R_i + R_e)\left(1 + \left(\frac{p\Omega}{\omega_p}\right)^2\right)} \cdot \Omega, \tag{1}$$

where K_t is the generator torque constant, K_e is the generator back electromotive force (EMF) constant, R_i is the internal phase resistance, R_e is the external load resistance on the windings [24]. At low angular speeds ($\Omega \ll \omega_p/p$), equation (1) reveals viscous damping behaviour given by

$$T \approx \frac{K_t K_e}{R_i + R_e} \cdot \Omega \tag{2}$$

With damping constant c, given by,

$$c = \frac{K_t K_e}{R_i + R_e}. \tag{3}$$

Hence, the damping behaviour of a Direct Current (DC) Permanent Magnet (PM) generator can be assumed linear, with viscous damping constant c described by equation (*3*), which can be altered based on the external resistance R_e [8]. Whilst Figure 2 represents the external generator load R_e as a simple resistor, the load can represent the total resistance of the power electronic circuitry used to store the energy from the generator. There exist many rectification circuits in literature to store the irregular electrical energy from the generator. For instance, designs range from simple diode bridge rectification circuits as in [26] or [27], to more optimised DC conversion circuits such as Synchronous Magnetic Flux Extraction (SMFE), which use less diodes and are hence more electrically power efficient [28]. However, the design of the electrical circuitry is out of the scope of this thesis and will not be further examined. An indirect drive EHSA system utilises a transmission mechanism to transform the linear relative motion between the wheels and car body to rotational movement to drive a generator, which often doubles as an amplification mechanism [12].

Direct drive systems on the other hand, do not make use of rotational permanent magnet electric generators such as the one in Figure 2. Instead, their designs involve linear permanent magnet generators. When such a generator is connected to an external resistance, the device becomes a linear mechanical damper. A direct drive system can therefore be directly substituted for a conventional telescopic viscous automotive damper. There is no need for a mechanism to convert linear motion into rotation to drive a rotary electric generator. Karnopp et al. [29] show analytically that a single-phase coil of total length l in a magnetic field B will produce a damping force F proportional to the speed of the coil with respect to the magnetic field $\dot{x}$ given by

$$F = \frac{B^2 l^2}{R_i + R_e} \cdot \dot{x}. \tag{4}$$

Note the similarity of equation (*2*) and (*4*) reflect that the generator constants K_t and K_e are related to the constant B and l. From equation (*4*), the damping coefficient can be altered by means of the external resistance R_e, similar to the rotational generator [29]. As explained in [29], the linear electrical generator variant used in direct drive system has inherent performance limitations relating to an increased mass relative to their rotational counterparts.

2.2.1. Direct Drive Electromechanical Shock Absorbers

Most literature involving the design of direct drive systems is usually focussed on the best magnet arrangement to increase the magnetic flux density gradient per unit mass in addition to the coil design and layout [30-32]. The design challenge is to achieve sufficient damping force and peak power generation while maintaining acceptable magnet and coil mass. This is because excessive unsprung suspension mass in a vehicle can significantly diminish ride quality [33]. Furthermore, it can even contribute considerably to the total mass of the car which decreases fuel efficiency. The magnetic flux

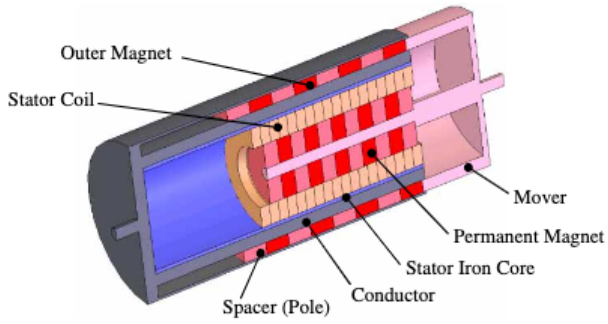

Figure 3: Linear (direct drive) electromagnetic damper design with double layer of permanent magnets and spacers [5].

density gradient of a magnet stack can be increased by introducing spacers between magnets to decrease the effect of flux cancellation between the opposite polarity ends of the magnets as shown in Figure 3. Equal thickness of magnets and conductive spacers has been shown to maximise efficiency with up to 60% increase in output power in test bench studies by [5]. Doubling the magnet amount is another common simple method of increasing the amount of magnetic flux lines permeating the coil (although this has obvious impacts on weight) [34].

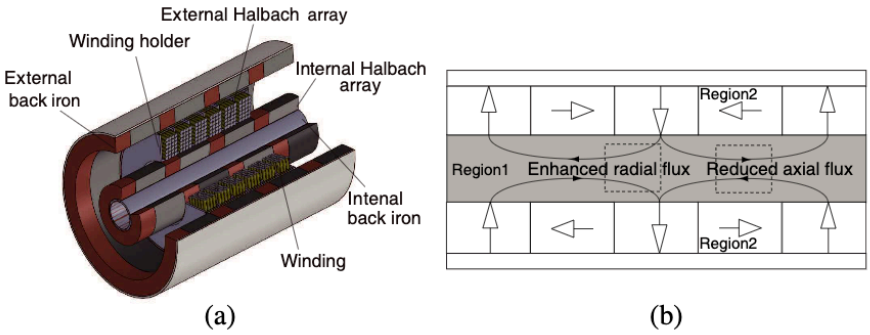

Figure 4: Dual Halbach array linear (direct drive) electromagnetic damper schematic (left) and magnet polarity arrangement of Halbach array showing flux lines (right) [7].

Furthermore, the superior electromagnetic coupling[1] and low mass of *Halbach arrays* compared to other magnet arrangements has attracted considerable attention in vibration energy harvesting (not limited to vehicle dampers) [7, 35-37]. A Halbach array configuration with consecutive magnets rotated by 90 degrees, intensifies the magnetic flux on one side of the array and attenuates to almost zero on the opposing side (as illustrated in Figure 4). This allows the entire available flux to be concentrated in the coil, thereby decreasing the total required permanent magnets and overall mass [36].

The prototype in Figure 4 could achieve good damping performance and its size was optimised through magneto-static analysis of the magnetic field, however no simulations involving stochastic inputs which mimic road excitations such as those discussed in section 4.3 were implemented [7]. In a more recent study, Duong et al conducted built and tested a PM Halbach array direct drive damper with spacers between magnets. The optimised coil/magnet design could harvest between 339.95 to 96.68 W of power for a vibration speed of RMS 0.25 ms^{-1}. However, the design experiences a detent 'cogging force' as the various coil phases move past the magnetic poles of the Halbach array [38], causing an uneven

[1] Electromagnetic coupling refers to the ability of an electromagnetic field to transfer its energy by inducing a charge or voltage in a conductor or circuit.

damping force throughout the damper stroke. The authors predicted this would cause negative effects on safety and driving comfort.

In general, a greater number of coil windings increases the power generated, however a limit exists when the added internal resistance of the lengthy coil begins to dissipate too much energy as discussed by [12]. An optimal relationship between the radial coil thickness and magnet thickness for direct drive EHSA can be obtained analytically given physical parameters of the design [34]. Furthermore, the use of multiple phases of coils decreases the amount of EMF potential which is cancelled compared to a single coil design. In a 4-coil design, Tang Lin et al showed that 26 to 33 W of electrical power could be generated with up to 1680 - 2142 Nsm^{-1} of damping force at a RMS damper velocity of 0.25 ms^{-1}. A typical passenger car will have a shock absorber damping ratio of around 1500 Nsm^{-1} as a reference [34].

2.2.2. Indirect Drive Electromechanical Shock Absorbers

Indirect drive EHSA designs mainly focus on the mechanism which increases the coil speed with respect to the magnets, or involve the design of custom electric generators which are optimised to the damping application [12]. Examples of these mechanisms which convert the linear bidirectional motion of the suspension into rotational motion include rack and pinion gears, ball screws, belt drives, cable drives and hydraulic/pneumatic actuator mechanisms driving rotational generators. Additionally, clutching mechanisms are used to convert bidirectional motion to unidirectional motion.

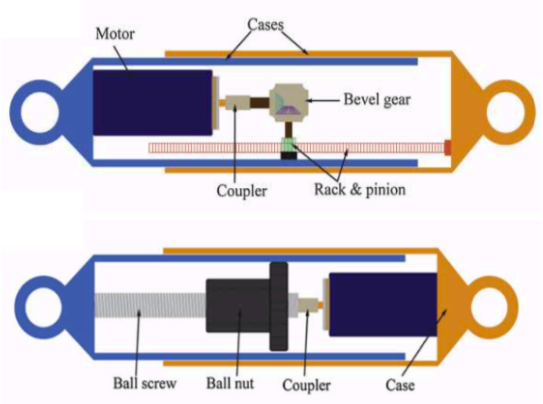

Figure 5: Generalised illustration of rack-pinion (top) and ball screw (bottom) indirect damper design [1].

Ball screw mechanisms typically perform well under low frequency excitation, however the additional inertial mass can result in decreased handling and ride comfort [39]. Yongchao et al. fitted a small sedan with their experimental ball screw and permanent-magnet DC brushless EHSA and found that ride quality at high frequencies was significantly worse than the control test with conventional passive

suspension [40]. Poor high frequency performance is frequently reported for ball screw mechanisms [41, 42] and simple rack-pinion designs resembling Figure 5. Furthermore, the backlash [2] and prolonged use is reported to cause fatigue and even premature failure of components [43]. For instance, in early prototypes by [21], the rack teeth of a simple rack and pinion mechanism were found to wear out and break quickly. The rack–pinion-based EHSA was tested on a *Chevrolet Suburban and* confirmed that a peak power of 67.5 W and average power of 19.2 W could be harvested on "fairly smooth" campus roads at a speed of 48 kmh^{-1}. A total energy conversion efficiency of 56% was calculated given vibrations under 0.5 Hz.

To address the poor high frequency performance of the rack–pinion-based mechanism by [21], the same authors proposed an updated EHSA with a motion mechanism which they call the *Mechanical Motion Rectifier (MMR)* [9] as illustrated in Figure 6.

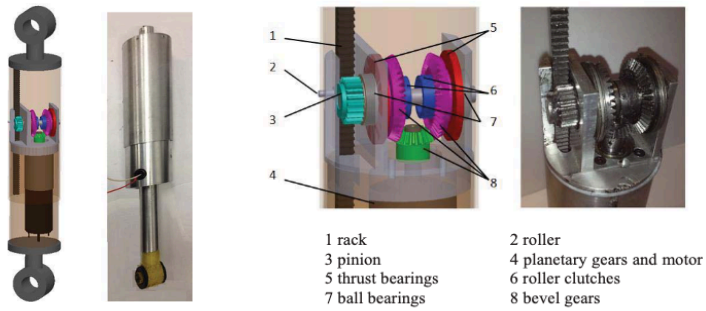

Figure 6: The rack-pinion based EHSA design with MMR for better high frequency response [9].

The system reduces the impact forces caused during oscillation by converting the bi-directional oscillatory motion of suspension into unidirectional rotation of the electrical generator. The elimination of backlash which occurs during inversion of the generators rotation simultaneously increases the reliability of the damper and increases its efficiency due to the reduction of static friction. The MMR consists of two roller clutches (i.e. one way bearings) embedded in two bevel gears which both mesh with a third bevel gear on the generator shaft. The generator shaft can rotate at a relatively steady velocity during irregular vibrations. Road tests showed that the EHSA with MMR mechanism achieved a reported 62% energy efficiency at high frequencies (compared to 30-45% obtained from the earlier prototype without the MMR).

Some ball screw based designs, such as a design by Liu et al. also explore the addition of clutching mechanisms to convert reciprocating suspension vibration into unidirectional generator rotation [4]. The design is illustrated in the figure below.

[2] Backlash refers to the clearance or lost motion in a mechanical mechanism due to gaps or flexure in its parts [30].

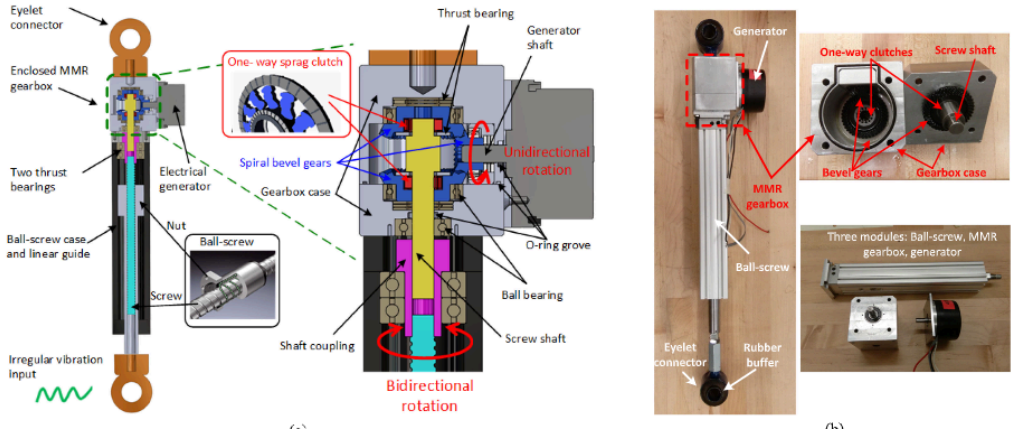

Figure 7: MMR clutching mechanism with ball screw design [4].

The EHSA by Liu et al. displayed 70.1% mechanical efficiency on bench tests at low frequency and 51.9% efficiencies at "high" frequency vibrations of 4Hz with a 3 Ohm external load. Electrical efficiencies were not given. The EHSA was only testes up to 5 Hz, with efficiency decreasing with increased excitation frequency.

Cable and belt drive systems have also been explored with the objective of decreasing the inertial mass of the moving mechanism. For instance, Bowen et al. designed a cable and pulley-based mechanism to drive an electric rotational generator. A full car *Simulink* model of the *Renault Twizy 45* (a small 445kg city car) and four of the EHSA was created which considered parameters such as the elastic modulus of steel and cable and inertial properties of the subcomponents, which other studies rarely consider Renault with four of the of the EHSA was created could. Simulations showed that 105 W RMS could be harvested on city roads at speeds between 20 – 30 kmh^{-1} [44].

A unique rotational electromagnetic EHSA by *Audi*, named *eROT* was announced in press release by the *Audi Media Centre* in 2017 [45]. A horizontally mounted alternator is connected via linkages directly to the rear suspension wishbones, replacing the traditional upright telescopic dampers, as depicted in Figure 8. Although the original article by *Audi* has been retracted, external media sources state that the *eROT* system responds quickly with minimal inertia and an active control algorithm allows for variable damping. The average power output during testing on German roads was supposedly between 100 to 150 W, from 3 W on a freshly paved road to 613 W on a rough secondary road in total (two *eROT* units combined) [2].

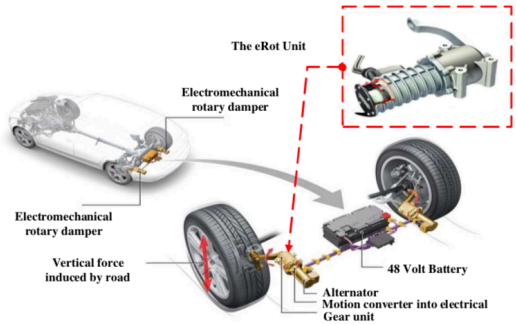

Figure 8: Audi eROT EHSA system [2].

A patent filed in 2014 describes a dual planetary gearbox transmission with a specific transmission ratio designed to achieve adequate generator speed for effective voltage induction for both "small and long wave oscillations" [46]. The transmission of high torques from the wheels to the generator is a great use of a planetary gearbox. Planetary gearboxes typically have high torque transmitting ability, due to the multiple engagements in its gearing and compact and efficient power transmission [10]. *Audi* has not released any follow up information on their *eROT* design since 2017. However, there has been development in recent literature involving the use of planetary gearboxes for EHSA systems.

Figure 9: The Rotary Regenerative Shock Absorber (RRSA) design by [8] showing linkage positioning on a McPherson strut geometry and individual components, including two stage planetary gearbox and generator rotor and stator.

Test bench studies revealed that the rotary damper design by [8] could achieve an efficiency between 27.69% and 59.86%, which is dependent on the shunt external resistance on the generator. In [47], another two stage rotary damper was built, with a greater focus on the planetary gearbox design. The mechanical gearbox design was guided by the expected load input spectrum which was determined through a quarter car simulation with a stochastic ISO 8608 grade C road profile input [48]. Researchers at the same university built the power electronics to store the energy from the rotary machine with a quoted electrical efficiency of 82%, resulting in a total regenerative shock absorber efficiency is 34.2% [49].

3. Problem Statement

The literature review confirms the feasibility of employing PM electrical generators as dampers in automotive suspension. Studies showed that a PM electrical generator with its terminals shunted by an external load resistance would act as an eddy current damper with controllable damping coefficient.

A distinction could be drawn between direct and indirect EHSA designs. Indirect designs showed the most promising theoretical and experimental results, however motion conversion mechanisms such as ball screws and rack and pinon gears proved be unreliable and be a weak point in most real-world prototypes. Recent designs of rotational energy harvesting dampers with planetary gearing showed impressive energy harvesting potential, with experimental prototypes of dampers reaching energy conversion efficiencies above 50% and a total efficiency above 30% when including the power electronic circuitry for storing energy.

However, the amount of energy which can be harvested from a vehicle suspension system is dependent on the vehicle and the surface it is travelling on. There is limited empirical research which investigates the true viability of real-life EHSA prototypes, as applied to a real-life vehicle. This report will make a novel assessment of the viability of developing an EHSA system for the *University of New South Wales* (*UNSW) Sunswift VII solar vehicle*. A realistic simulation model of the *UNSW Sunswift VII solar vehicle* will be built as a case study to determine how much energy is lost under realistic driving conditions in the existing viscous fluid dampers of the vehicle. Along with the findings from the literature review, this study provides an insight towards the realistic energy harvesting potential of this *Sunswift VII vehicle*.

4. Creating a Vehicle Model

4.1. Modelling the Dynamics of a Vehicle

A quarter car, two DOF model is a simplified representation of a vehicle's suspension system and is a common bench model in studies involving the design and control of vehicle suspension [50]. The two degrees of freedom consist of the vertical motion z_s of the sprung mass m_s and vertical motion z_u of the unsprung mass m_u, as illustrated in Figure 10b. These two masses are obtained through a 'lumped mass modelling' approach, which involves simplifying the vehicle's structure into a set of discrete masses connected by springs and dampers. The unsprung mass represents everything connected rigidly to the wheel (e.g. the tyre, spokes, rim, hubs, suspension linkages etc.) and the sprung mass represents the combined mass of the vehicle chassis. In quarter car modelling the sprung mass is the corner weight of the car minus the unsprung mass. The spring k represents the elastic deformation of the suspension, while the damper c represents the energy dissipation due to the damping effect of the suspension. The tire is also approximated as a single spring, which represents the tire's elastic deformation due to the forces acting on it.

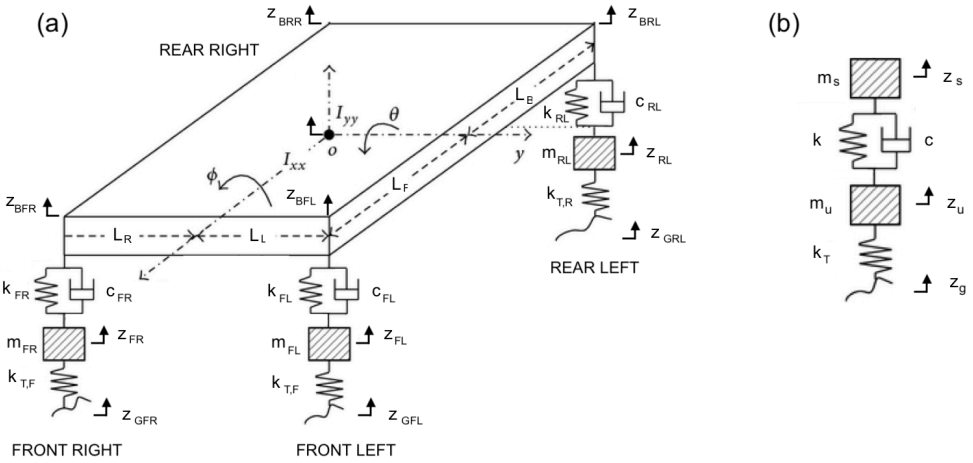

Figure 10: Diagram showing seven degree of freedom lumped mass, full-car model (a) and two degree of freedom lumped mass, quarter car model (b).

The quarter car model in Figure 10b is not computationally intensive to simulate and is able to reasonably predict the effects of road disturbances on the vehicle's vertical acceleration and displacement, however the accuracy due to the simplification of the model is limited [51]. From *Newton's laws*, the quarter car model is governed by the following system of equations:

$$\begin{bmatrix} m_u & 0 \\ 0 & m_s \end{bmatrix} \begin{pmatrix} \ddot{z_u} \\ \ddot{z_s} \end{pmatrix} + \begin{bmatrix} c & -c \\ -c & c \end{bmatrix} \begin{pmatrix} \dot{z_u} \\ \dot{z_s} \end{pmatrix} + \begin{bmatrix} k_T + k & -k \\ -k & k_T \end{bmatrix} \begin{pmatrix} z_u \\ z_s \end{pmatrix} = \begin{bmatrix} k_T \\ 0 \end{bmatrix} z_g$$

This can be written equivalently as,

$$M\begin{pmatrix}\ddot{z_u}\\ \ddot{z_s}\end{pmatrix} + C\begin{pmatrix}\dot{z_u}\\ \dot{z_s}\end{pmatrix} + K\begin{pmatrix}z_u\\ z_s\end{pmatrix} = K_0 z_g$$

(5)

where M is the mass matrix, C is the damping matrix, K is the spring stiffness matrix and $K_0 = [k_T\ 0]^T$. The system in (5) can be modelled using the state space representation, with state vector $Z = [z_u\ z_s\ \dot{z_u}\ \dot{z_s}]^T$ and state equation given by

$$\dot{Z} = AZ + Bz_g,$$

(6)

where,

$$A = \begin{bmatrix} 0 & I \\ -M^{-1}K & -M^{-1}C \end{bmatrix},$$

(7)

and

$$B = [0 \quad M^{-1}K_0].$$

(8)

The output of the system is discussed in section 5. Although preliminary simulations were conducted in *Simulink* using the quarter car model, a full car dynamic model, as illustrated in Figure 10a provides a more comprehensive representation of a vehicle's suspension system. It includes interactions between the front and rear suspension, as well as the effects of vehicle roll and pitch. This level of detail can help to more accurately predict vehicle handling, ride comfort, and stability. The full car model features a degree of freedom for the vertical motion of each wheel, as well as the vertical motion, pitch and roll of the chassis (sprung mass). The full set of differential equations can be found in the Appendix.

There is another issue with the state-space approach described by equations (7) - (8). As discussed in section 4.4, an accurate model of the *Sunswift VII* car requires non-linear damping behaviour. Problematically, a system with variable damping as a function of velocity does not satisfy the fundamental Linear Time-Invariance (LTI) assumption of state-space modelling. In the quarter car example, this results in a state dependent damping matrix C. The Appendix illustrates attempts of using the state space form of the full car time-variant model raising solver warnings in *Simulink*. This issue is solved by abandoning the state-space modelling approach and instead representing the system as shown in Figure 11.

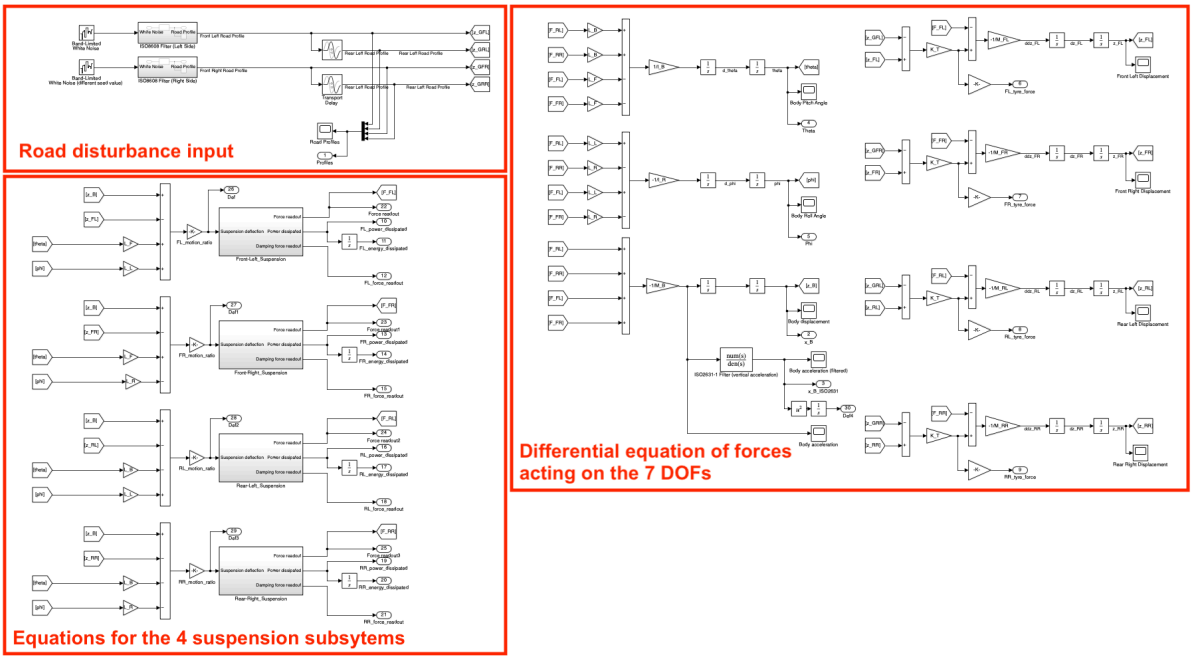

Figure 11: Layout of the complete full vehicle car model in Simulink, highlighting the three major sections of the simulation set up.

Each of the seven differential equations governing the seven degrees of freedom of the full car is represented in the Simulink model shown Figure 11 (right) as a separate subnetwork using *Simulink* blocks. For example, the network regarding the vertical motion of the front left wheel is created by multiplying the wheel mass by the sum of acting forces to produce the left front wheel acceleration. The displacement is obtained using two integration blocks in series.

The parameters used in the full car model are known. The lengths L_L, L_R, L_F, L_B are the wheelbase dimensions from the centre of gravity known from the vehicle CAD model. The total chassis mass M_B is the addition of the mass of the body of the car (which was weighed using car scales) and four 70kg passengers. The unsprung masses $M_{FL}, M_{FR}, M_{RL}, M_{RR}$ were also individually weighed using scales. The spring stiffness of the tyres K_T is supplied by the manufacturer, as explained in section 4.5 and the suspension spring stiffness $K_{FL}, K_{FR}, K_{RL}, K_{RR}$ and damping were also experimentally determined as outlined in section 4.4. Lastly, the vehicle pitch inertia I_θ and roll inertia I_ϕ was estimated by assuming the car chassis as a rectangular prism with known mass and dimensions. The contribution of the additional inertia to the car of four seated 70 kg passengers and the vehicle battery were added separately. The dimensions used for Inertia calculations are shown in the appendix. The following table states the value of all parameters.

Parameter	Value
CoG to left wheels distance, L_L	0.81 m
CoG to right wheels distance, L_R	0.81 m
CoG to front wheels distance, L_F	1.772 m
CoG to rear wheels distance, L_B	1.348 m
Measured car mass (no passengers)	572 kg
Approx. mass of four passengers	70*4 kg
Front left wheel mass (unsprung), M_{FL}	9 kg
Front right wheel mass (unsprung, M_{FR}	9 kg
Back left wheel mass (unsprung, M_{RL}	24 kg
Back right wheel mass (unsprung, M_{RR}	24 kg
Total chassis mass (sprung), M_B	786 kg
Body pitch inertia, I_θ	982.3 kgm^2
Body roll inertia, I_ϕ	245.2 kgm^2
Front suspension spring rate, K_{FL}, K_{FR}	31600 Nm^{-1}
Back suspension spring rate, K_{RL}, K_{RR}	72000 Nm^{-1}
Front tyres spring rate, $K_{T,F}$	262300 Nm^{-1}
Rear tyres spring rate, $K_{T,R}$	255200 Nm^{-1}
Front suspension motion ratio, MR_F	1.00
Rear suspension motion ratio, MR_R	1.09

Table 1: Table of simulation parameter values.

The motion ratio of the suspension refers to the ratio of vertical wheel displacement to the displacement of the shock absorber and is a result of the geometry of any mechanical linkages connecting the suspension to the wheel. In simulation, the input displacement, velocity and acceleration to the suspension subsystem must be divided by the motion ratio and the resulting force produced by the suspension is also divided by the motion ratio MR.

$$MR = \frac{wheel\ displacement}{suspension\ displacement}$$

An equivalent method of adjusting the simulation parameters according to the motion ratio is by introducing two new quantities; a *wheel spring rate* K' (the spring rate the wheel experiences) and

wheel damping rate C' (the damping rate the wheel experiences) which is a function of the *spring rate* of the suspension K and the *damping rate* of the suspension C [52, 53]*:*

$$K' = \frac{K}{MR^2}; \qquad C' = \frac{C}{MR^2}.$$

Every *Simulink* simulation performed in this report is configured using a variable time-step solver which modifies the size of the steps taken during a simulation, adjusting it to enhance accuracy when a system's states undergo rapid changes and to minimize unnecessary steps when the states are changing at a slower rate. The integration algorithm is set to be automatically determined by the simulation.

4.2. Vehicle Model Verification

A simple verification approach could be used to confirm that the Simulink full-vehicle model produces correct output. The displacement of each degree of freedom is calculated through the double integration of its acceleration. The acceleration is found using *Newton's laws* from the sum of forces acting the respective degree of freedom and its mass quantity. Therefore, the correct displacement of each degree of freedom is only correctly found if the forces acting are correctly represented and the acceleration is correctly integrated. For example, by applying simple ground displacement inputs, the unsprung mass will only displace correctly if all forces acting on it are correctly expressed. Figure 12 shows that the steady-state roll induced by lifting the left wheels 0.5m off the ground, produces the expected vehicle body displacement of 0.25m (due to the vehicle being left-right symmetrical). This same process was used to excite all degrees of freedom and verify the simulation response.

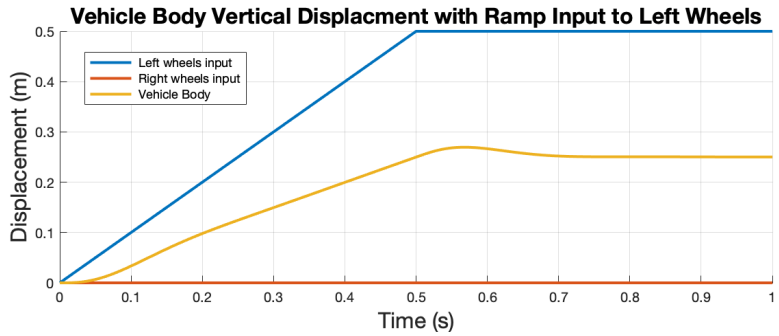

Figure 12: Vehicle body displacement response to a ramp input with saturation at 0.5m at both left wheels.

4.3. Modelling Road Profiles

The main disturbance into a vehicle suspension system is the roughness of a road's surface [54]. To accurately predict the response of vehicle whilst driving on a given road, it is necessary to correctly characterise the road's surface. A two-dimensional slice of road taken along an imaginary longitudinal line is a road profile, which can be modelled statistically. Given a vehicle is travelling at a constant velocity, road roughness is a stationary and ergodic stochastic process which follows a *Gaussian* probability distribution with a mean of zero. These conditions make it possible to describe the statistical properties of a road profile using a Power Spectrum Density (PSD) function. Furthermore, the constant velocity power spectral density satisfies the statistical properties of white noise and allows an appropriate transfer function to be used to model the statistical magnitude of road surface roughness in time domain models. The road surface displacement power spectrum can be defined as:

$$S_{PSD}(n) = S_{PSD}(n_0)\left(\frac{n}{n_0}\right)^{-m}, \tag{9}$$

where $S_{PSD}(n)$ represents the PSD (m^3) as a function of the spatial frequency n (m^{-1}), which is the inverse of wavelength, λ (m) [55]. Lambda, λ, represents the wavelength of a given wave signal present in the road profile, and its inverse, n, represents the number of wavelengths per meter. The irregularity coefficient $S_{PSD}(n_0)$ (m^3) is the road surface PSD at reference spatial frequency $n_0 = 0.1$ (m^{-1}). The constant m represents the degree of 'waviness' of the road. The waviness defines the slope of the log-log plot in Figure 14. Existing literature has found realistic values for m to be in the range of $1.75 < m < 2.25$ but is commonly equal to 2 [55]. Furthermore, for the purpose of simulating realistic road profiles the vehicle speed should be considered. Given a constant vehicle velocity u (ms^{-1}), the time frequency, f (s^{-1}), is related to the spatial frequency, n, by $f = un$. Thus, the PSD $S_{PSD}(n)$ with spatial frequency is converted to the time frequency PSD $S_{PSD}(f)$ by,

$$S_{PSD}(f) = \frac{1}{u} \cdot S_{PSD}(n). \tag{10}$$

Given that angular frequency is equal to $\omega = 2\pi f$ and using equation (9) and (10), the PSD $S_{PSD}(\omega)$ of the road roughness can be written as:

$$S_{PSD}(\omega) = (2\pi)^2 S_{PSD}(n_0)\, n_0^2 \frac{u}{\omega^2 + \omega_0^2}. \tag{11}$$

A lower cut-off angular frequency ω_0 is added as a lowpass filter to limit the attenuation of vanishingly small frequencies to be finite [54]. From the *Wiener-Khinchin* theorem [56], given an input PSD function $H_{PSD}(\omega)$ to a system, the output PSD function $S_{PSD}(\omega)$ can be calculated using the frequency response function of the system $G(\omega)$ such that

$$S_{PSD}(\omega) = |G(\omega)|^2 \, H_{PSD}(\omega). \tag{12}$$

If the input function $H_{PSD}(\omega)$ is the PSD of a white noise signal $w(s)$, with unit power spectrum density $H_{PSD}(\omega) = 1$, then the time domain displacement disturbance $x_g(t)$ to a vehicle tyre can be obtained from (11) and (12), using the first order linear shape filter

$$G(\omega) = \frac{2\pi n_0 \sqrt{S_{PSD}(n_0) \cdot u}}{\omega_0 + j\omega} \tag{13}$$

such that in the time domain,

$$x_g(t) = \mathcal{L}^{-1}\left(w(s) \cdot \frac{2\pi n_0 \sqrt{S_{PSD}(n_0) \cdot u}}{\omega_0 + s} \right) \tag{14}$$

given that $s = j\omega$ has no real component and $\mathcal{L}^{-1}$ is the inverse *Laplace* transform [25]. This equation allows an equivalent road profile of any given surface roughness to be modelled using the road surface irregularity coefficient $S_{PSD}(n_0)$, its corresponding reference spatial frequency n_0 and the vehicle velocity u. The following figure shows how equation (14) can be implemented in a *Simulink* model.

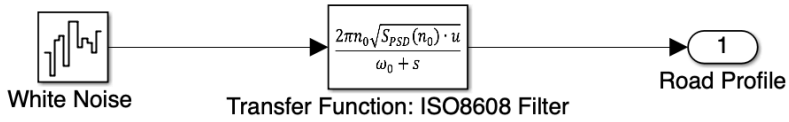

Figure 13: Simulink Implementation of ISO8608 White Noise Filtration Method.

The international standard *ISO 8608 - Mechanical vibration — Road surface profiles - Reporting of measured data* presents a uniform road classification scheme based on the value of the road irregularity coefficient $S_{PSD}(n_0)$. The standard assigns a grade A – H for roads based on a range of the degree of roughness [3]. The coefficients are often reported in either angular spatial frequency units (rad/m) or spatial frequency units (cycles/m). This report will use the spatial frequency values with reference spatial frequency $\mathrm{n_0} = 0.1\ \mathrm{cycles/m}$ as reported in the ISO 8608 standard [3]. The values are reported as follows.

Table 2: ISO 8608 Road Roughness Power Spectral Density [3].

Road Class	ISO 8608 Road Roughness Power Spectral Density		
	Lower Limit	Geometric Mean	Upper Limit
	PSD in Spatial Frequency Units, $S_{PSD}(n_0) \times 10^{-6}$ m³		
A	-	16	32
B	32	64	128
C	128	256	512
D	512	1024	2048
E	2048	4096	8192
F	8192	16384	32768
G	32768	65536	131072
H	131072	262144	-

*$n_0 = 0.1\ cycles/m$ [3]

For example, Figure 14 (top) shows the generated displacement road profile for a ISO8608 mid-grade A road with PSD $S_{PSD}(n_0) = 16 \times 10^{-6}$ m^3. Figure 14 also shows that the power spectrum of the generated road profile corresponds to the theoretical PSD of the ISO 8608 standard, as represented by equation (9). This result verifies the white noise filtration method in *Simulink* for obtaining road profile excitations.

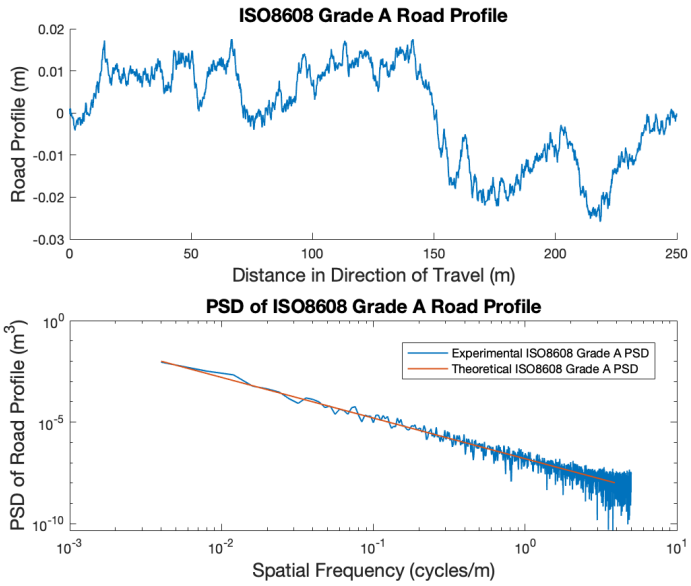

Figure 14 ISO8608 grade A road profile (top) and corresponding power spectrum in spatial frequency units (bottom).

However, when applying road excitations given by ISO8608 it is extremely important to validate that the simulation parameters (vehicle velocity and road irregularity coefficient) are consistent with the spectrum properties of real roads. A study by Múčka et al. found that many scientific literature based

their findings on incorrect or inconsistent simulation parameters which leads to inflated results [57]. For example, the maximum realistic vehicle velocity as a function of ISO 8608 road class, as determined by Múčka et al., is given in the table below. Furthermore, the qualitative categories of roads presented in the ISO 8608 classification are based of experimental data from the 1960s to 1970s and it is evident that they have not been updated to suit modern roads. For instance, class B and C roads (which are labelled as *good* and *regular* in the original ISO 8608 standard) are nowadays considered lower quality paved roads [57].

Table 3 Maximum recommended vehicle velocities for ISO8608 road grades and their proposed description by [57].

ISO 8608 Road Class	**A**	**B**	**C**	**D**	**E**
Description	Highways and Motorways		District to Country Roads	Unpaved Roads	
v_{MAX} (km/h) for ride comfort threshold value, a_{wz} = 1.2 m/s^2	> 100	> 100	~ 31	~ 8	~ 3
v_{MAX} (km/h) for safety threshold	> 100	> 100	~ 59	~ 15	~ 4

The description of road classes determined by Múčka et al. was done using a simulation approach. Unfortunately, no empirical reports of road roughness data of Australian roads which relate back to the ISO8608 standard could be found. Hence, a small study was conducted to compile the survey data from Austroads technical reports on the deterioration of Highways and Main roads at test sites around the Australian continent. The *Austroads* collective includes Australian and New Zealand transport agencies at all levels of government [58]. The compiled data includes site details such as the road surface type, location, survey date and roughness measure. The roughness measure is reported using the International Roughness Index (IRI), which together with the ISO8608 standard is one of the most used roughness indices for evaluating road surfaces. From [59], the IRI can be converted to a ISO8608 PSD coefficient using

$$IRI = 2.21\sqrt{S_{PSD}(\Omega_0)}$$

where $S_{PSD}(\Omega_0)$ has reference angular spatial frequency of $\Omega_0 = 1$ rad/m. The conversion to spatial frequency units is simply

$$S_{PSD}(n_0) = 16 \cdot S_{PSD}(\Omega_0)$$

as explained in the ISO8608 standard [3]. The results of the study are compiled in the Appendix, and the average roughness across the surveyed Australian Highways is shown below.

Table 4: Australian road roughness statistics compiled from Austroads data.

Australian Test Site Average		
Quantity	**PSD, $S_{PSD}(\mathbf{n_0})(\times \mathbf{10^{-6}})\ \mathbf{m^3}$**	**ISO8608 Grade**
Average	19.60	A
Std. Dev.	17.76	-
Min.	2.26	A
Max.	100.91	B

Furthermore, the average roughness of Australian roads which are constructed using Asphalt, like the Stuart Highway on which the *UNSW Sunswift Solar Car* will be competing during the 2023 *Bridgestone World Solar Challenge* is tabulated below.

Table 5: Australian asphalt road roughness statistics compiled from Austroads data.

Australian Asphalt Only Site Average		
Quantity	**PSD, $S_{PSD}(\mathbf{n_0})(\times \mathbf{10^{-6}})\ \mathbf{m^3}$**	**ISO8608 Grade**
Average	12.54	A
Std. Dev.	8.69	-
Min.	3.21	A
Max.	32.51	B

The results show that, on average, Australian Highway roughness is almost in the middle of the ISO 8608 Grade A range, with the worst surveyed roads at the upper end of the Grade B range. Additionally, the roughness distribution of Australian Highways made from Asphalt sits almost entirely in the Grade A range, with the roughest surveyed road being only marginally over the 32×10^{-6} m^3 boundary. This conclusion supports the categorical classification made by Múčka et al. in table 5 above.

4.4. Damper Model of Sunswift Solar Vehicle Suspension

In most literature involving the modelling of vehicle suspension or control design of intelligent suspensions, a vehicle is represented using lumped parameter models. The vehicle consists of the sprung mass (chassis), unsprung masses (wheels, axles, linkages, etc), and elastic and dissipative elements. The vehicle suspension system is commonly represented by a spring with linear stiffness characteristic and a damper with a linear damping characteristic [50]. The linearity assumption of the vehicle suspension system provides analytic simplicity. However, the shock absorbers used in real cars typically do not follow a perfectly linear damping behaviour. During the design phase of a vehicle, manufacturers typically run various handling simulations using different available dampers in order to improve the ride and handling characteristics of the vehicle [60]. The damping characteristic can be described by how the force produced by the damper relates to the relative velocity between the upper and lower mounts of the damper. During the compression stroke (also known as Jounce), the top and bottom ends of the damper move towards each other. Conversely, the top and bottom ends of the damper move away from each other during the expansion stroke (also known as rebound).

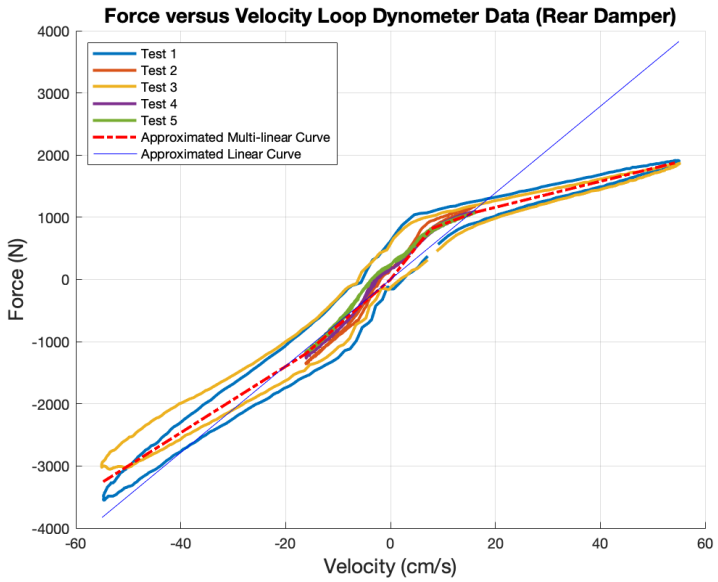

Figure 15: Force-velocity characteristic of rear damper installed in the Sunswift VII Solar Vehicle, based off the dynameter data from Bilstein.

The force-velocity characteristic of the rear monotube damper in the *Sunswift VII Solar Car* is shown in Figure 15, where positive velocities are indicative of jounce and negative values refer to rebound. The data was obtained by mounting the damper (with the spring coil-over removed) onto to a shock dynometer machine at the suspension manufacturer *BILSTEIN*. The machine cyclically compresses and extends the damper and records the exerted force, over the displacement and velocity of the damper. Multiple tests are repeated for increasing amplitudes and velocities. Three low speed and two high speed tests are shown in Figure 15. Hysteresis is the gap between the jounce and rebound strokes, resulting in

different values of force for the same damper velocity [60]. Hysteresis in the damper results in a variation of the force produced for the same set of velocities while the damper is accelerating and $\frac{dv}{dt} > 0$, and during the deceleration phase when $\frac{dv}{dt} < 0$. Factors contributing to the hysteresis include inertial properties of the oil in the damper, oil compressibility, air compressibility and volumetric expansion of the damper cylinder [60]. The graph also features a 'knee' at roughly 7 cms^{-1}, where the force tapers down. It is very common for compression damping to be lower than rebound. When encountering a bump in compression, the spring is loaded, and lower damping results in less force being transferred to the vehicle chassis. Most of the energy stored in the spring is then dissipated in the rebound stroke. A good multilinear approximation of the damping behaviour is included in red. The linear curve (in blue)

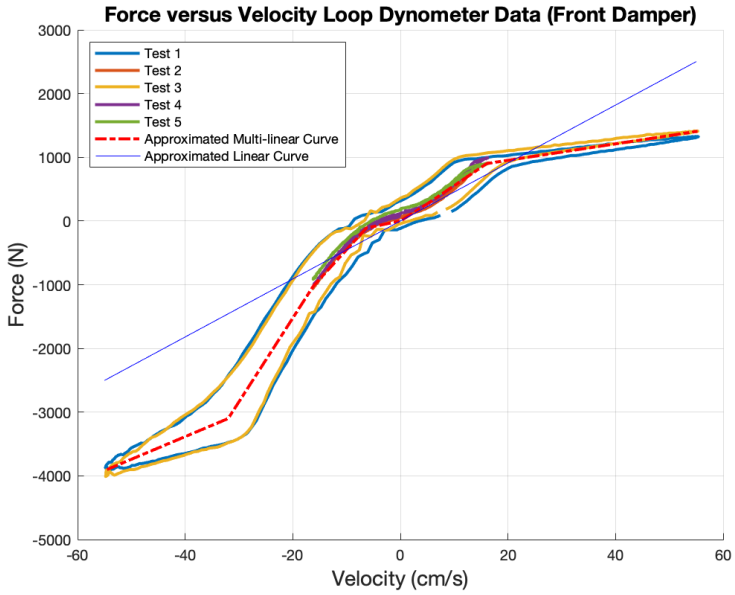

Figure 16: Force-velocity characteristic of front damper installed in the Sunswift VII Solar Vehicle, based off the dynometer data from Bilstein laboratory.

is a good approximation for the low-speed behaviour of the damper and is tangent to the low-speed compression curves around the origin but becomes inaccurate at higher velocities. The gradient of the linear curve is the damping coefficient typically quoted in datasheets.

The same tests conducted on the front damper of Sunswift VII Solar vehicle are shown in Figure 16. The front damper exhibits a digressive damping characteristic in both compression and rebound. This means that the damping force increases sharply for low velocities and then at a lower rate for higher velocities. Figure 16 also shows that the linear approximation becomes very inaccurate for absolute velocities above 20 cms^{-1}. Conversely, the red multi-linear curve for both dampers represents an approximation of the ideal force-velocity characteristic of each damper. Both curves can be described using data in the lookup table of Table 6 which corresponds to the multilinear curve in Figure 15 and Figure 16. The *non-linear translational damper* block in the *Simscape™ Driveline* toolbox can be used to represent a non-linear damper in Simulink simulations. The block takes the lookup tables as inputs

and uses a linear interpolation method to represents forces between the range of the values specified in the lookup table.

Table 6: Lookup table for Sunswift VII front damper (left) and rear damper (right).

Velocity (cm/s)	Force (N)
-54.6	-3902.0
-32.0	-3100.0
-16.2	-1019.0
-6.3	-110.0
0.0	0.0
5.0	271.0
16.1	902.0
55.2	1408.0

Velocity (cm/s)	Force (N)
-54.8	-3253.0
-16.2	-1195.0
0.0	0.0
7.7	814.0
16.1	1078.0
54.7	1885.0

The dampers are bench tested to a maximum of ± 55 cm/s, which is the maximum velocity of the dynometer. Whilst the exact damping characteristics beyond the ± 55 cm/s is not known exactly; a linear extrapolation method is used which follows the same gradient at the left and right fringes of the graph in Figure 15 and Figure 16. This is a valid assumption because the valving of the damper does not change past the final transition in gradient, as explained by the manufacturer.

4.5. Tyre Model of Sunswift Solar Vehicle

The vehicle tyres can be modelled as an ideal spring with negligible damping. The spring force of the *Bridgestone* solar car tyres used on the vehicle exhibit a simple linear relationship with the vertical corner weight of the vehicle as shown in Figure 17. This information is supplied by the manufacturer.

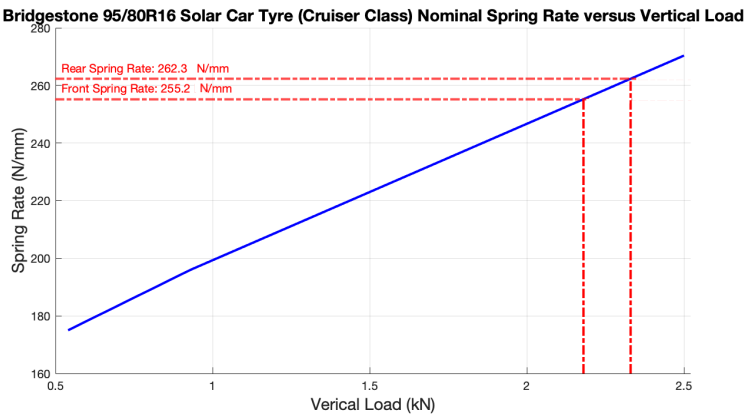

Figure 17: Tyre spring rate versus vertical load for Bridgestone 95/80 R16 solar car tyre.

5. Simulation Output Evaluation Criteria

There are two main criteria used to evaluate the dynamic response of a vehicle in literature involving suspension modelling. The first criterion consists of an assessment of ride comfort and the second is an assessment of vehicle handling and safety.

5.1. Ride Comfort

The degree of comfort felt by passengers is subjective and dependent on many factors such as ergonomics, acoustics, temperature and humidity. However, studies show that human comfort greatly depends on the level, direction and frequency content of whole-body vibrations felt by the passenger [50]. For example, the human body is most sensitive to vertical vibrations in the frequency range of 4-8 Hz as these correspond to the resonant frequencies of organs in the abdominal cavity. On the other hand, the sensitivity frequency range for horizontal vibrations is between 1 to 2 Hz [50]. The international standard *ISO 2631 – Mechanical vibration and shock — Evaluation of human exposure to whole-body vibration* aims to quantify whole body vibration in relation to human health and comfort [33]. This report will consider mainly the vertical vibrations felt by the passenger, as the full car model used does not consider horizontal forces induced on the vehicle. For a person in a seated (or standing) position, the frequency weighted root means square acceleration a_{wz} is defined in the standard by

$$a_{wz} = \sqrt{\sum_{i=1}^{37} \left(W_{k,i} \times a_{iz}^{RMS}\right)^2}. \quad (15)$$

The constants weightings $W_{k,i}$ are defined on page 7 of the standard for 37 one-third-octave frequency bands which give more relative weight to the frequency ranges where the human body is most sensitive to vibrations. A suspension system should be tuned to maintain suitable limits for vibrations within the frequency ranges of concern to achieve optimal ride comfort [61]. For the purpose of applying the frequency weighting method in a *Simulink* simulation, it is convenient to make a suitable approximation using a stable transfer function. Many lower order filter approximations have been designed by authors such as [62] for practical applications such as controller design where higher order transfer functions can introduce added computational complexity. A common second order filter $W_k^{(2)}(s)$ used in works such as [63, 64] is given by

$$W_k^{(2)}(s) = \frac{50s + 500}{s^2 + 50s + 1200}.$$

(16)

However, as shown in Figure 18 (in blue), equation (16) is not a good approximation to the weightings W_k. Using the *Matlab Filter Design Toolbox* function *iirlpnorm* and the procedure described in [62], second through to fifth order continuous time filters which approximate the desired frequency response can be found. Equation (17) gives the fifth order approximation used in this report.

$$W_k^{(5)}(s) = \frac{87.72s^4 + 1138s^3 + 11336s^2 + 5453s + 5509}{s^5 + 92.6854s^4 + 2549.83s^3 + 25969s^2 + 81057s + 79783}.$$

(17)

As shown in Figure 18, the fifth order filter in equation (17) gives a much better approximation (in green).

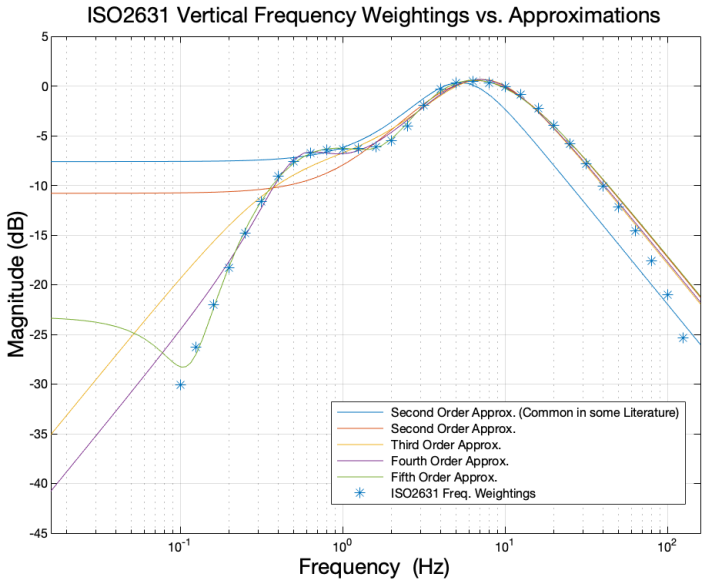

Figure 18: Second through to fifth order human vibration-sensitivity filters as approximations to the ISO2631 frequency weightings (also marked).

Equation (17) can be directly applied in *Simulink* as a continuous time filter for the chassis vertical acceleration a_s, resulting in the ISO 2631-weighted chassis acceleration $a_{2631}(t)$.

$$a_{2631}(t) = \mathcal{L}^{-1}\left(a_s(s) \cdot W_k^{(5)}(s)\right)$$

(18)

The RMS value of the resulting signal, a_{wz}, is calculated from the simulation output in the time domain for simulation time T and can be used to roughly gauge the passenger comfort.

$$a_{wz} = \sqrt{\frac{1}{T}\int_0^T \left(a_{2631}(t)\right)^2}$$

(19)

Although the acceptable values of the frequency weighted acceleration (or frequency weighted vibration amplitude) are subjective, the ISO standard provides some guidelines, as shown in Table 7.

Table 7: ISO 2631 Comfort Ratings.

Weighted RMS Acceleration, a_{wz}	**Nominal Comfort Rating (ISO 2631)**
<0.315 ms^{-2}	Not uncomfortable
0.315 ms^{-2} to 0.63 ms^{-2}	A little uncomfortable
0.5 ms^{-2} to 1 ms^{-2}	Fairly uncomfortable
0.8 ms^{-2} to 1.6 ms^{-2}	Uncomfortable
1.25 ms^{-2} to 2.5 ms^{-2}	Very uncomfortable
>2 ms^{-2}	Extremely uncomfortable

Based on the data in Table 7, a maximum permittable weighted RMS acceleration a_{wz} of 1.6 ms^{-2} is used for simulations. Experimental studies by Cantisani et al. found that the comfort rating depends on the type of vehicle, for example, a passenger on a motorbike can be subjected to higher vibration content under the same comfort level [65, 66]. Although the proposed comfort limit of 1.6 ms^{-2} is relatively high, the vehicle simulated in this report is a race car in which comfort is of lesser priority. Furthermore, this is only an indicative measure.

5.2. Vehicle Handling

When travelling over a very uneven surface, extreme vibrations may cause the wheels of the vehicle to lose contact with the road surface, which results in a loss of control during manoeuvres such as cornering, braking or accelerating [50]. The road handling performance index ξ can be defined as the ratio of dynamic force between the tyre and ground and the static corner weight of the car W_i at each ith wheel.

$$\xi_i = \frac{k_{T,i}\left(z_{u,i} - z_{g,i}\right)}{W_i}$$

(20)

Due to the parameters z_u and z_g being defined from the equilibrium position, when the tyres are loaded under the weight of the car, if the ratio exceeds one then the spring force of the tyre pushing the car upwards exceeds the weight of the car and traction will be lost. Thus, ξ can be interpreted as follows: In this study, a road handling performance index of $\xi = 1$ at any point during a simulation represents a break condition, and the simulation is terminated.

Table 8: Interpretation of the dynamic to static tyre force ratio ξ.

Range	Meaning
$\xi < 1$	The vehicle experiences traction.
$\xi = 1$	The vehicle is likely to experience no traction.
$\xi > 1$	The vehicle is likely to lose ground contact.

5.3. Mechanical Suspension Constraints

It is important to monitor the total suspension deflection at each wheel. If the simulation indicates that a shock compresses past its physical compression length (bottom out) or extends past its extension limit (top out), then the vehicle is at risk of damage. Furthermore, this situation presents a linearity constraint of the Simulink model. For example, at maximum compression, any additional upward displacement of the wheel would be directly transferred to the vehicle chassis, thus nullifying the spring/damper elements in the vehicle model. The simulation cannot accurately represent this condition. For these reasons, Table 9 shows the hard limits which are introduced in the *Simulink* simulations for both suspension extension and compression. The values are provided by the manufacturer of the shock.

Shock Length	Front Shock	Rear Shock
Full Compression	257mm	252mm
Ride Length	303mm	294mm
Full Extension	333mm	365mm

Table 9: Sunswift VII Suspension length constraints.

5.4. Power Dissipation within the Dampers

The maximum harvestable energy in the vehicle suspension is equal to the amount which is dissipated due to the work done by the viscous damping force in each damper [25]. The instantaneous power dissipated is equal to the damping force F_d times the damper velocity v_d:

$$P = F_d \cdot v_d.$$

If a damper is ideal and linear with damping coefficient c, the damping force is $F_d = cv_d$. Using the suspension motion ratio M, the damper velocity v_d can be expressed in terms of the unsprung and sprung mass velocity by $v_d = M(\dot{z_s} - \dot{z_u})$, such that the instantaneous power dissipated in the damper is given by

$$P_{linear\ damping} = cM(\dot{z_s} - \dot{z_u}) \cdot M(\dot{z_s} - \dot{z_u})$$

$$= c\big(M(\dot{z_s} - \dot{z_u})\big)^2.$$

However, given that the damping behaviour of the Sunswift VII vehicle is non-linear with respect to velocity (as approximated by the values in Table 6), the damping force F_d is a function of the damper velocity v_d such that

$$P_{non-linear\ damping} = F_d(v_d) \cdot \big(M(\dot{z_s} - \dot{z_u})\big) \quad (21)$$

Equation (21) can be implemented numerically in Simulink. As described in section 4.4, the vehicle suspension subsystem is modelled as a physical *Matlab Simscape system*. The force $F_d(v_d)$ is found using the *Ideal Force Sensor* Simscape Block directly each time step. The dissipated power is then calculated by multiplying the force by the suspension stroke velocity $\big(M(\dot{z_s} - \dot{z_u})\big)$.

6. An Analytical Note regarding Performance Criteria

An intriguing relationship which relates the RMS ISO 8608 road roughness coefficient to the RMS harvested power was found by Lei Zuo et al. analytically for a quarter car model with linear suspension damping [25]. In linear systems theory, the H2-norm $\|H\|_2$ can be interpreted as the output RMS value of a system with transfer function $H(j\omega)$ in response to white noise.

$$\|H\|_2^2 = \frac{1}{2\pi}\int_0^\infty \mathrm{trace}\big(H^*(j\omega)H(j\omega)\big)d\omega$$

Therefore, the RMS suspension velocity, $\sigma_{\dot{x}_s-\dot{x}_u}$ can be found given that $H(j\omega)$ is the transfer function from the ground velocity to the suspension velocity in a quarter car model, and the road roughness velocity is a constant intensity white noise signal. The authors define the rough roughness coefficient $S_{PSD}(\upsilon_0)$ in terms of a reference spatial frequency $\upsilon_0 = 1/2\pi$ cycles/m, which is different to the definition used in this report. The RMS suspension velocity was found in terms of the suspension damping coefficient c, vehicle velocity u and tyre stiffness k_T to be

$$\sigma_{\dot{x}_s-\dot{x}_u} = \frac{\sqrt{\pi S_{PSD}(\upsilon_0)uk_T}}{c},$$

and given that suspension damping force is linear with damping coefficient c, the RMS power dissipated in the damper P_{RMS} is expressed as:

$$P_{RMS} = c\big(\sigma_{\dot{x}_s-\dot{x}_u}\big)^2 = \pi S_{PSD}(\upsilon_0)uk_t. \qquad (22)$$

This is a remarkable result that suggests that the average power dissipated in the damper is proportional only to the vehicle velocity u, the road roughness $S_{PSD}(\upsilon_0)$ and the tyre damping k_t. The average dissipated power is apparently independent of unsprung mass, sprung mass and suspension damping c and stiffness k. Unfortunately, finding a direct conversion of equation (22), to an equation which uses the convention of road roughness coefficient $S_{PSD}(n_0)$ with reference spatial frequency n_0 (which is used in this paper) is difficult. Furthermore, a limitation of equation (22) is that the vehicle is approximated as a quarter car model with linear suspension damping that does not consider interactions between the front and rear suspension. It can, however, be used as an indication to the approximate results expected in a full car simulation.

7. Energy Dissipation Study

7.1. Energy Loss under ISO8608 Road Profiles and Constant Vehicle Velocity

In this section, the full-vehicle dynamic model is combined with the ISO8608 based road model input excitation, non-linear suspension model, tyre model as well as constraint criteria of ride comfort, vehicle handling and suspension deflection. The same randomly generated road profile is used as the input to the front and back wheels, with a time delay t_0 given by $t_0 = (L_F + L_B)/u$, where u is the vehicle velocity and $L_F + L_B$ is the front-to-back wheelbase distance. The left and right sides are generated from a different white noise signal, as shown in Figure 19. These conditions can excite all degrees of freedom of the model.

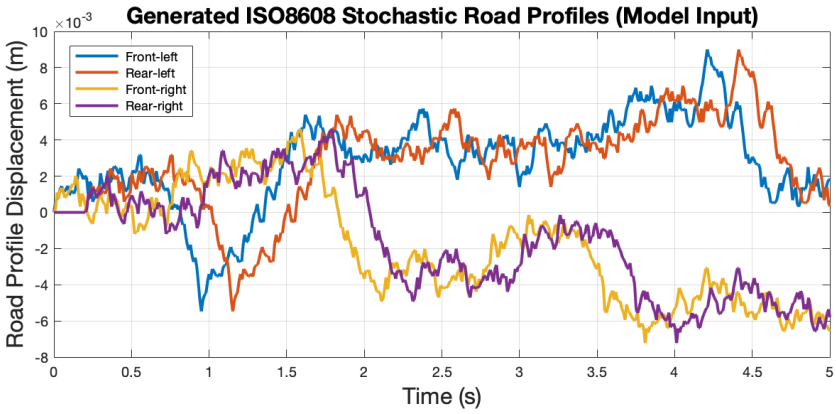

Figure 19: Example of ISO8608 Grade A road profiles with input delay to the rear wheels.

A *Matlab* script (shown in the Appendix) was then written to conduct a systematic sampling approach of various vehicle velocities u and road roughness coefficients $S_{PSD}(n_0)$. The output quantity of interest is the average (RMS) power dissipated in the suspension dampers. A sample set of vehicle velocities (depicted in Figure 20 and was chosen up to the maximum vehicle velocity of 140kmh^{-1}. For each vehicle velocity increment, the road roughness coefficient was increased from 1×10^{-6} m^3 in intervals of 10×10^{-6} m^3. During the simulation of each parameter set of u and $S_{PSD}(n_0)$, if any of the three constraint criteria were met, the simulation is terminated. If this condition was met, the same process is repeated from the last valid parameter set in increments of 1×10^{-6} m^3 for higher refinement. This process is sometimes referred to as a grid sampling method. Figure 20 shows a log-log plot of the result of this analysis for the average (RMS) power dissipated in each front suspension damper in the *Sunswift VII solar vehicle*. Figure 21 shows the results of the same analysis for the average (RMS) power dissipated in each rear suspension damper.

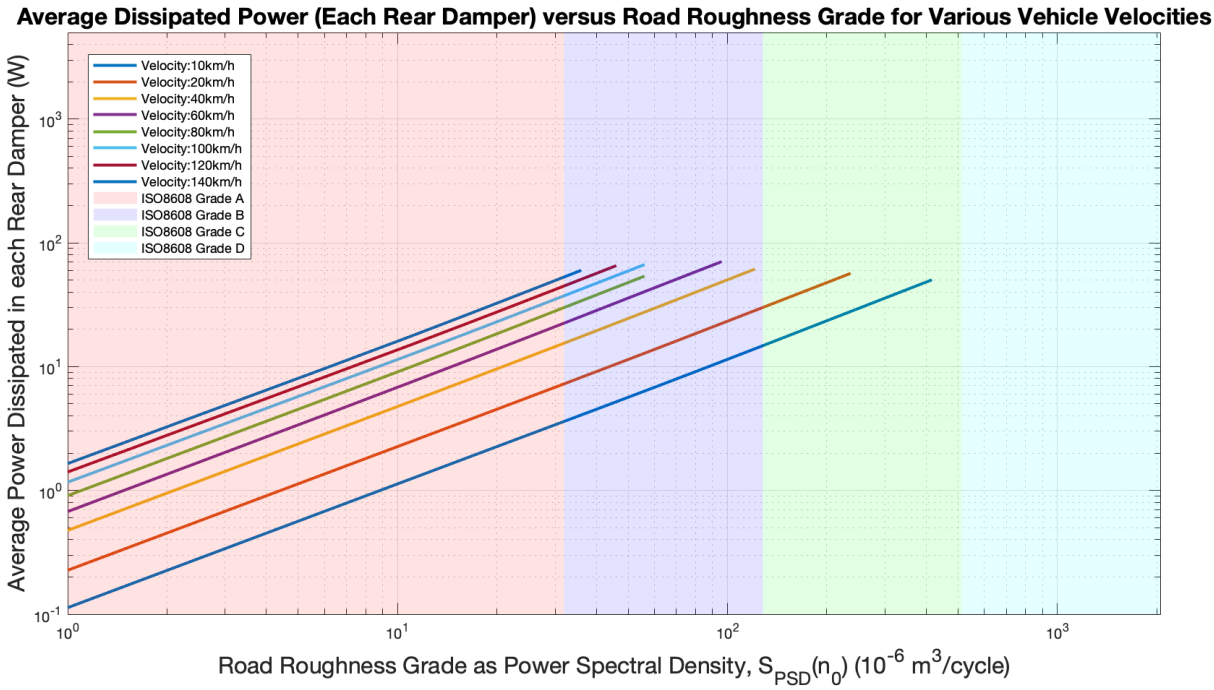

Figure 21: Average power dissipated in the rear dampers for varying vehicle speed and road roughness coefficient $S_{PSD}(n_0)$, showing the ISO8608 road grade classes as coloured bands.

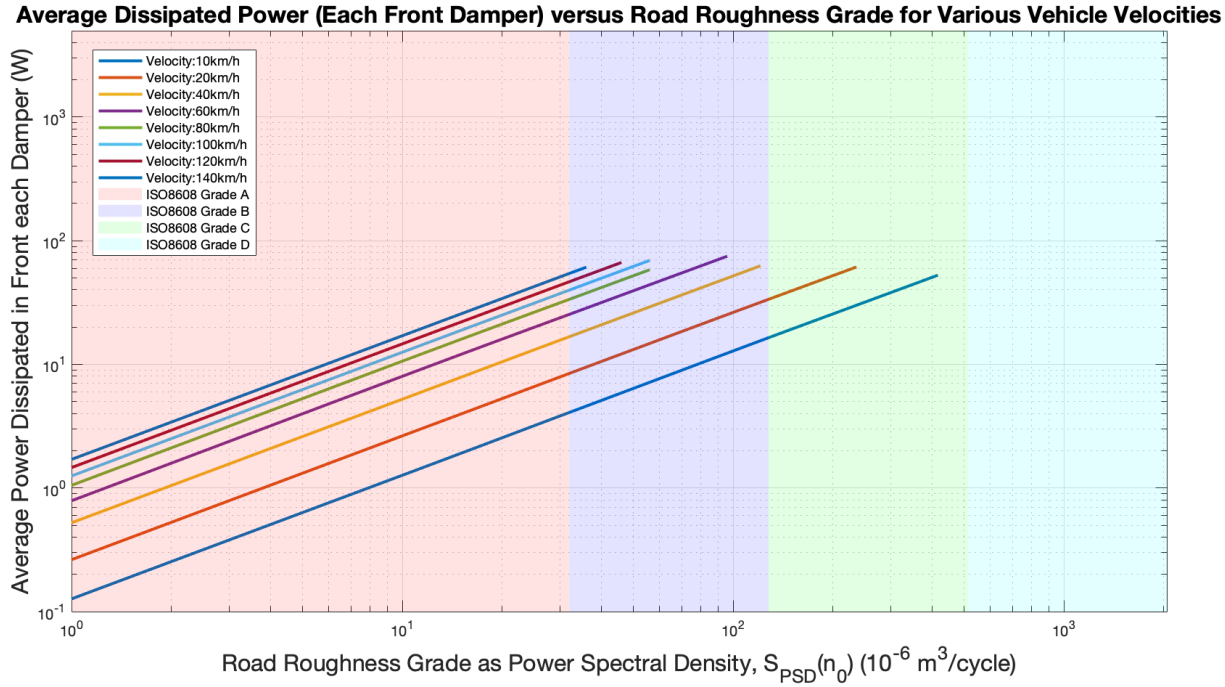

Figure 20: Average power dissipated in the front dampers for varying vehicle speed and road roughness coefficient $S_{PSD}(n_0)$, showing the ISO8608 road grade classes as coloured bands.

The coloured bands on the graphs in Figure 20 and Figure 21 indicate the ISO 8608 road classes A-D. The graph shows that the average power dissipated at any given velocity increases linearly with an increasing roughness coefficient. An increase in the vehicle velocity u results in an increased power for every given roughness. The cut-off point on each curve occurs when one of the constraint conditions are met. Notably, there is a maximum attainable power dissipation of on average ~63.38W per front

damper and ~60.56 W per rear damper (as shown in Table 10). Although this may not seem like an impressive figure, it is a considerable power loss in a high efficiency solar vehicle. In this study, the dominating constraint condition was always the road handling performance index ξ, which would consistently reach the limit $\xi = 1$ at some point in the simulation, just before the comfort limit of $a_{wz} = 1.6\ \mathrm{ms}^{-2}$ was reached. The suspension compression/ extension limit would always be reached last. This can be expected because the suspension stroke length is designed to be sufficient for regular operating conditions, representing $\xi < 1$, and should only reach its limit under large forces produced by obstacles on the road or violent vibrations.

Table 10: Maximum road-roughness coefficient (and ISO8608 class classification) for given vehicle velocities, with the corresponding dissipated power in the front and rear dampers.

Vehicle Velocity	Max. Roughness Coefficient, $S_{PSD}(\mathbf{n_0})(\times \mathbf{10^{-6}})\ \mathbf{m^3}$	ISO8608 Road Class	Power Dissipated per Damper (W)	
			Front	Rear
10	416	C	52.62	50.20
20	236	C	61.30	56.65
40	121	B	62.67	61.36
60	92	B	74.94	70.49
80	66	B	58.27	53.78
100	56	B	69.37	66.68
120	46	B	66.73	65.42
140	36	B	61.11	59.94
Average Power:			63.38	60.56

Table 10 summarises the maximum acceptable road roughness for the tested velocities, given the constraint criteria. Each row in the table represents the 'cut-off' point of each line in Figure 20 and Figure 21. Although the maximum dissipated power across different rows in Table 10 are similar, there does appear to be a maximum point for both the front and back power dissipation at the 60 kmh^{-1} mark. This could be an artefact of the low resolution of roughness coefficient increments which were used during the grid sampling methodology which was used during this study.

A more precise estimation could be obtained by decreasing the roughness coefficient increment (grid) size. Another potential for decreased precision, is that the same white noise signal was used to generate the road profile shown in Figure 19. Although the white noise signal filtered according to ISO 8608 based on the road roughness $S_{PSD}(n_0)$, the underlying white noise signal was the same throughout the study. The average power spectrum of a road profiles generated by different white noise signals is very similar in the frequency domain, and hence the average power dissipation can be expected to be very similar in the dampers for different white noise inputs.

The analysis in section 6 also shows that the average dissipated power is dependent only on the spectrum properties of the road profile signal. However, time domain properties of the signal such as the large peaks shown in Figure 19 have a direct impact on the constraint criteria such as the road handling performance index of $\xi = 1$, which will directly impact the precision of the cut-off point on each curve of the graphs in Figure 20 and Figure 21, and resulting maximum power values in Table 10. Therefore, an average of many different white noise profiles should be used to obtain more precise values. Unfortunately, this is extremely computationally intensive, and not feasible considering that the total simulation time to produce Figure 20 and Figure 21 was already more than an hour. The average maximum value of the power dissipation in the front and rear dampers across the entire velocity range in Table 10 therefore serves as a good compromise.

The relationship between the average dissipated power and vehicle velocity, given a constant road roughness was also investigated and plotted in Figure 22. Two ISO 8608 Grade A, and two ISO 8608 Grade B roads were simulated. The results showed that the power dissipated is proportional to the vehicle velocity, as was determined analytically by Lei Zuo et al. in section 6 for the quarter car model.

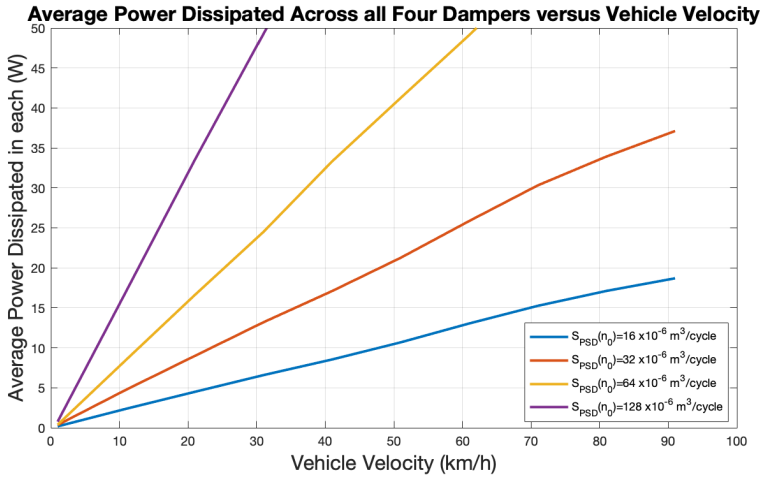

Figure 22: Average power dissipation across the front and rear dampers with under four constant road roughness coefficients versus the vehicle velocity.

7.2. Dimensionless Parameter Sensitivity Analysis

The analysis in the previous section provides an insight towards the harvestable power in the front and back suspension in the *Sunswift VII car*, with the nominal simulation parameters (defined in Table 1), in addition to the nominal suspension and tyre model. This section will examine the sensitivity of the RMS harvestable power, the RMS road handling performance index ξ, and the RMS ISO 2631 weighted vertical chassis acceleration under a change of the nominal simulation values. It is desirable to determine the sensitivity of the simulation parameters considering that there can be error in the nominal values.

In each set of figures, one parameter is changed within an acceptable range around the nominal value. The parameter set is then normalised by dividing by the nominal value, resulting in a dimensionless parameter set. In the same way, a dimensionless value is obtained for the three RMS performance quantities, by dividing by the performance of the nominal parameter set. For example, Figure 23 shows the effect on the front suspension performance and rear suspension performance of changing the front tyre stiffness only.

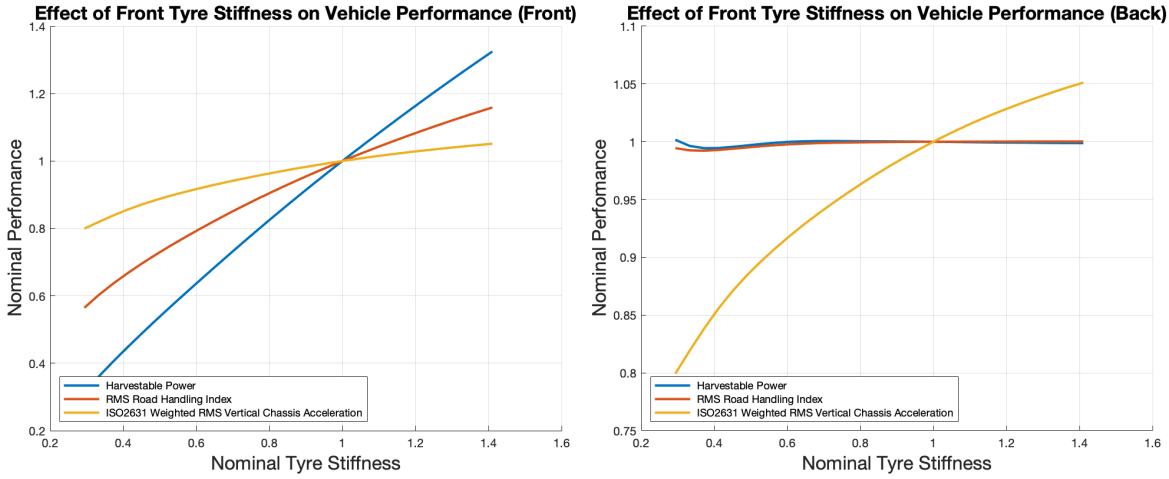

Figure 23: Dimensionless effect of front tyre stiffness on harvestable power, road handling performance and ISO 2631-weighted RMS chassis acceleration of the front suspension (left) and back suspension (right).

The results show that increasing the stiffness of the front tyres, increases the harvestable power, but also increases the RMS road handling index and RMS weighted chassis acceleration at the front suspension. For example, a 1.4x (40%) increase in front tyre stiffness from the nominal value results in a 32% increase in harvestable energy (desirable) but also a 16% increase in the RMS road handling index (undesirable), and 5% increase in the RMS weighted chassis acceleration (also undesirable). A higher harvestable energy is expected based on the analytical equation (*22*) by Zuo et al., which shows the tyre stiffness is proportional to power. Evidently the increased tyre stiffness causes increased movement of the chassis and wheel mass, as more force is transferred through the tyre for a given tyre

deflection. However, as illustrated in Figure 23 (right) the front tyre stiffness has little to no effect on the handling of the rear wheels and power harvesting potential of the rear wheels.

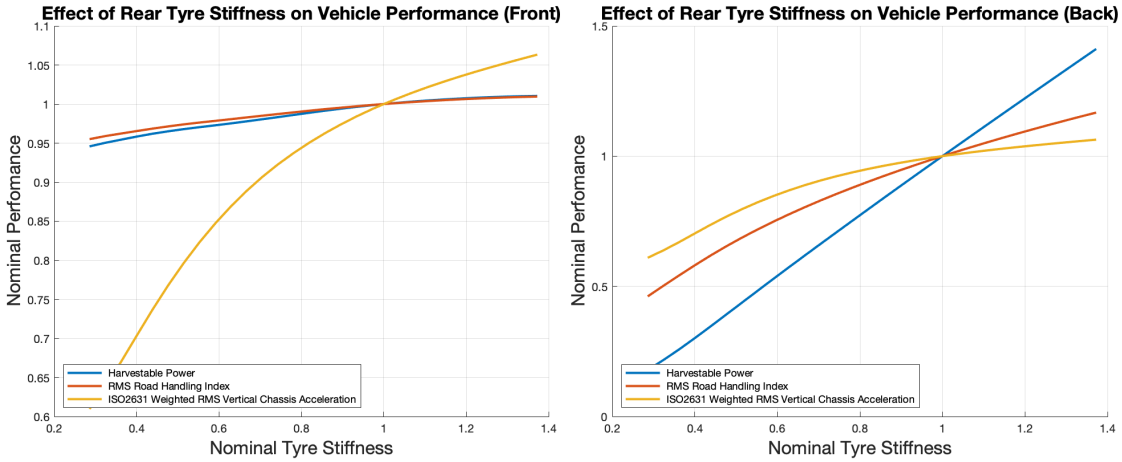

Figure 24: Dimensionless effect of rear tyre stiffness on harvestable power, road handling performance and ISO 2631-weighted RMS chassis acceleration of the front suspension (left) and rear suspension (right).

Figure 24 shows a similar analysis with a change of the nominal *rear* tyre stiffness and its effect on the front and rear suspension performance. The results show that a change in the rear tyre stiffness results in a similar change in the performance criteria of the rear suspension, as did changing the front tyre stiffness to the performance criteria of the front suspension in Figure 23. However, Figure 24 also shows a small change in the front suspension performance. For example, a reduction in rear tyre stiffness to 40% of the nominal value results in a reduction to 96% of the harvestable power in the front suspension and 97% RMS road handling in the front suspension. It can be concluded that due to the higher spring rate and mass of the rear wheels, a considerable amount of vibration energy is transferred through the chassis, thus impacting the front suspension.

Next, the graphs in Figure 26 show the effect of a change in the front wheel (unsprung) mass on both the front and rear suspension performance. Evidently, all the performance parameters are not as sensitive to the front unsprung mass change as they are to the tyre stiffness shown in the previous Figure 23 and Figure 24. A 2x (100%) increase in front wheel mass results in only a 4.2% increase in harvestable power, a 5.3% increase in ISO 2631 weighted chassis acceleration and 0.1% increase in road handling index. Hence, increased wheel mass is undesirable as the vehicle handling index increases comparatively more than the gain in harvestable power. The right-side graph in Figure 26 shows that the back suspension performance is not very sensitive to front wheel mass.

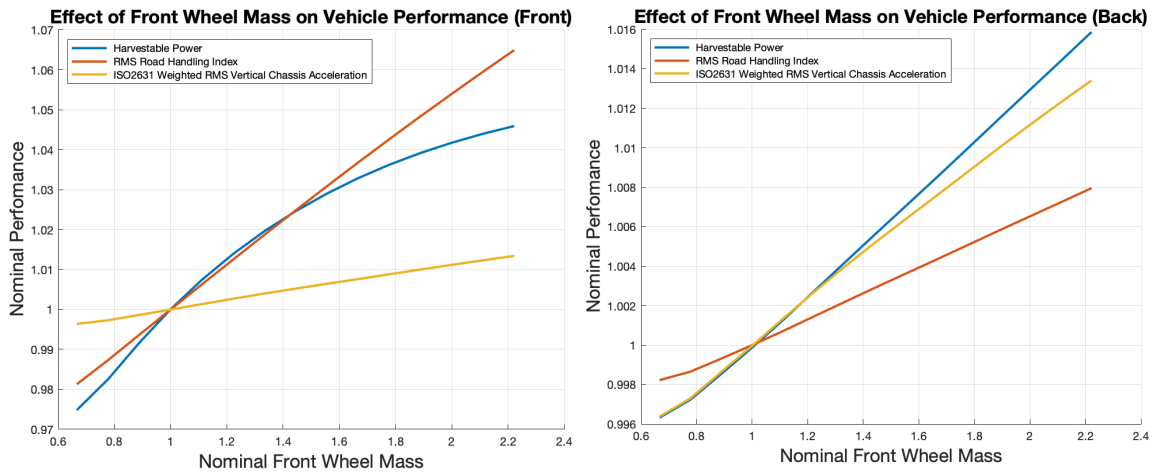

Figure 26: Dimensionless effect of front wheel (unsprung) mass on harvestable power, road handling performance and ISO2631-weighted RMS chassis acceleration on the front suspension (left) and rear suspension (right).

The small harvestable power change shown in the front suspension under the change in front wheel mass is contrary to what is suggested by the analytical equation (*22*) by Zuo et al. The analytical equation suggests that RMS harvestable power is independent of unsprung mass. This discrepancy is likely because equation (*22*) is based on an over-simplified quarter car model, whereas this simulation is that of a full car model. Furthermore, the white noise generated in Simulink is not actually "true white noise" as it must be band limited to be finite.

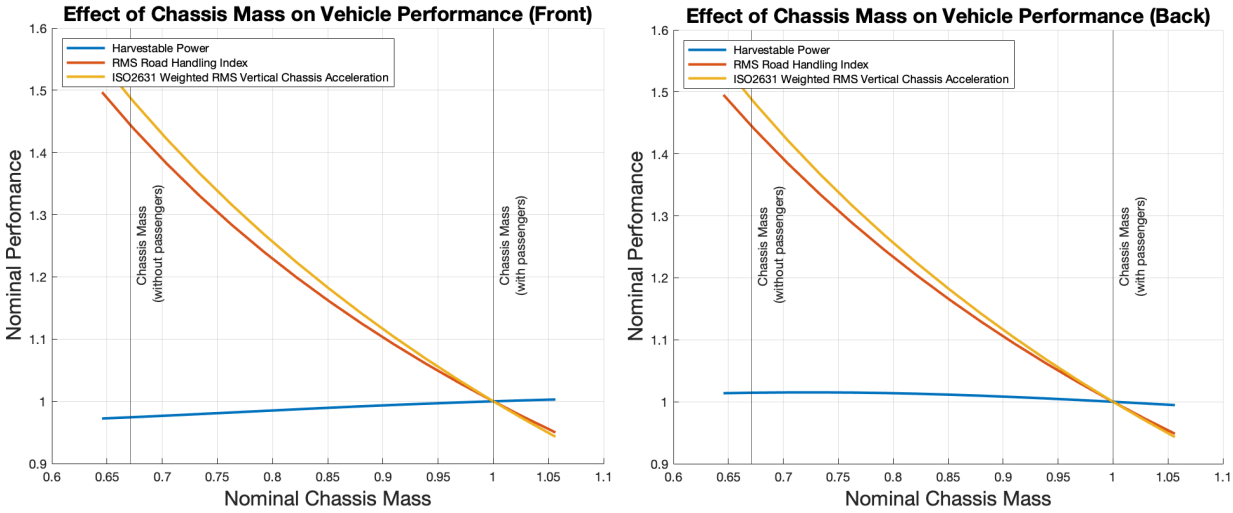

Figure 25: Dimensionless effect of chassis mass on harvestable power, road handling performance and ISO2631-weighted RMS chassis acceleration of the front suspension (left) and rear suspension (right).

The graphs in Figure 25 show the impact of increased vehicle chassis (unsprung) mass on the front suspension performance and rear suspension performance. The nominal chassis mass represents the fully loaded car with four 70 kg passengers. The vehicle chassis mass without any passengers (67% of the nominal mass) is also marked. Evidently, a larger chassis mass is desirable for better road handling and ride comfort. In fact, the vehicle would experience a 49% increase in weighted chassis acceleration and 45% increase in road handling index in the case of decreased vehicle chassis mass with no

passengers. It can be expected that an increased mass results in a decreased RMS acceleration because the mass is inversely proportional to acceleration. Similarly, an increase in chassis mass results in better handling because the static weight force pushing the car onto the ground is larger. Furthermore, Figure 25 shows that the harvestable power is not as sensitive to the chassis mass in both the front and rear suspension. Interestingly, there is a very small increase in harvestable power with an increase in chassis mass in the front suspension but a small decrease in harvestable power with an increase in chassis mass in the rear suspension.

Lastly, an analysis was done into the effect of changing the front suspension damping coefficient. In this study, the vehicle suspension is approximated to have ideal linear behaviour using nominal damping coefficient of 4550 Nsm^{-1} for the front suspension and 6960 Nsm^{-1} for the rear. These values correspond to the linear approximations of the vehicle dampers about the origin in Figure 15 and Figure 16. The front linear damping parameter is then altered. The results are shown in Figure 27.

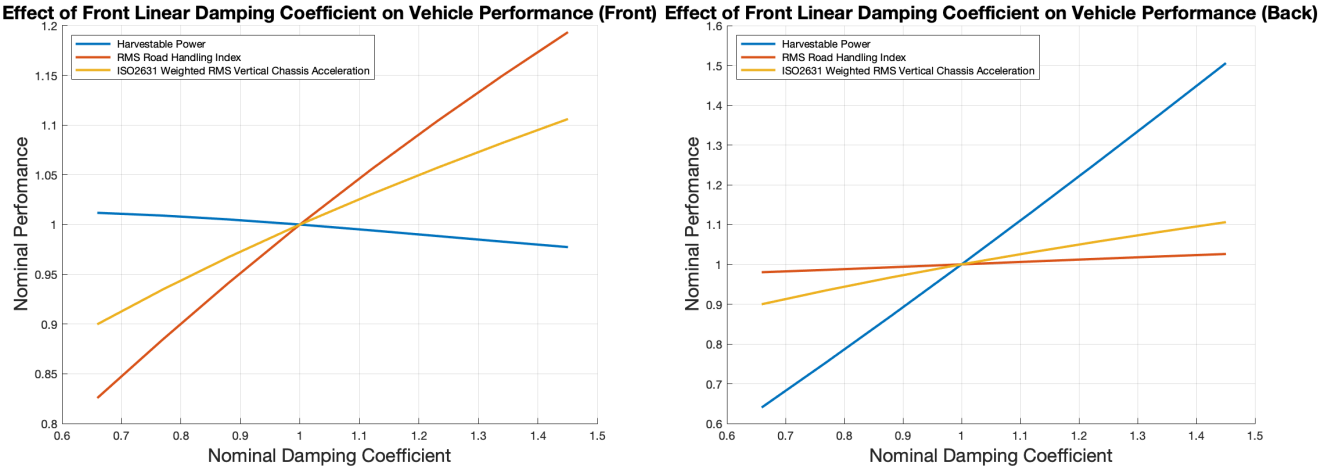

Figure 27: Dimensionless effect of linear front damping coefficient on harvestable power, road handling performance and ISO2631-weighted RMS chassis acceleration of the front suspension (left) and rear suspension (right).

Based on the analytical equation (*22*) by Zuo et al., the harvestable RMS power in the front damper is expected to be independent of the damping coefficient of the front damper. The graph in the left of Figure 27 partially supports this, because the harvestable power is relatively insensitive to the damping coefficient. The graph shows that an increase in the front damping coefficient of 40% results in 98% of the nominal harvestable power. The partial sensitivity is likely due inability of the quarter car model to reflect the full vehicle dynamics, or the limitations of the producing 'true' white noise in *Simulink*. Remarkably, the front linear damping rate has a drastic impact on the harvestable power in the rear damper, as shown in the right graph of Figure 27. This is likely because the increase in the front damping coefficient results in more force being transferred directly to the vehicle chassis, which is then dissipated in the rear suspension.

8. Experimental Data Acquisition

Verification studies of the Simulink model were conducted to show that the vehicle model produced the expected steady-state output under simple road profile input conditions such as ramp inputs. However, validating the simulation results in comparison to the real-life system is more difficult. In an ideal world, the same model input (such as an ISO 8608 road profile) could be applied to the simulated *Sunswift VII solar vehicle* and the real-life vehicle. The vehicle responses such as the RMS acceleration of masses or frequency responses in each case could then be compared with each other. Problematically, the ISO 8608 based road profiles are straightforward to generate in simulation, but they cannot simply be generated in real life. Conversely, it is also difficult to measure the profile of a real-life road without specialised equipment such as a laser profilometer. Due to these apparent challenges of directly validating the input-output relationship of the simulated model with the real Sunswift vehicle, an indirect validation approach was used instead, which made use of more accessible sensors. This process is described in section 9.

8.1. Construction of the Data-logging Equipment

The first attempt to obtain data from the vehicle included installing two *100mm MoTeC linear potentiometers* in parallel with front suspension of the vehicle. The right side of Figure 28 shows one of the linear potentiometers installed on the front-left existing suspension element in the vehicle. The potentiometers can continuously measure the length of the suspension stroke between 0-100mm by providing a linear voltage output between 0 to 5 V. The voltage output signal was initially recorded using a custom-built *Arduino Uno* powered data logger, which presented multiple design challenges in itself. For example, the inbuilt analog-to-digital converter (ADC) measures voltages on its analog input pins relative to its supply voltage, which has a rated tolerance of up to 5% of the nominal 5 V value.

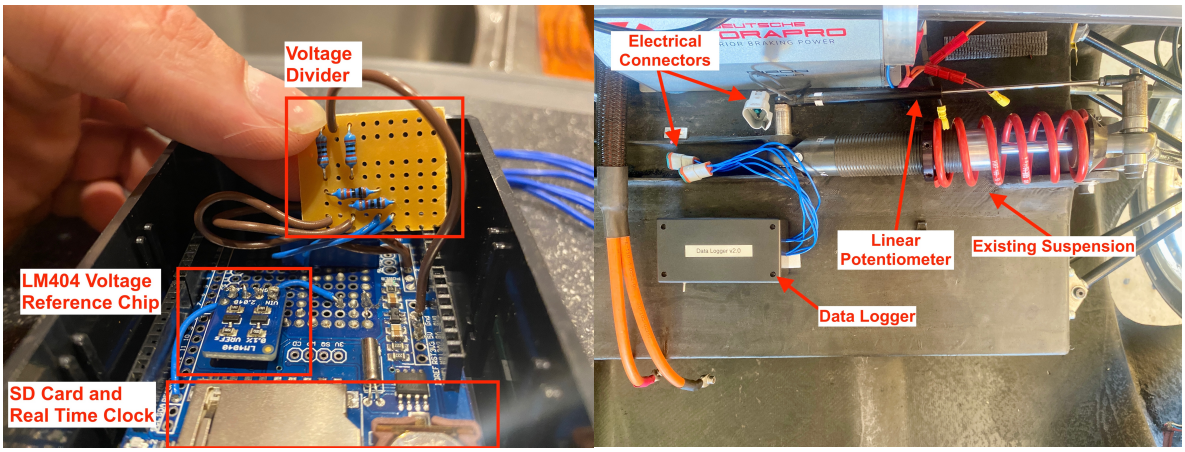

Figure 28: Inside view of the first version of a purpose-built Arduino Uno powered data logger (left) and data logger installed on Sunswift Solar vehicle, showing mounting of linear potentiometer (right).

More accurate sensor measurements could be obtained using a voltage reference chip, which could provide a stable and accurate 4.096 V voltage source (with only 0.1% tolerance) that is independent of the Arduino's supply voltage. Furthermore, a voltage divider needed to be constructed to scale the maximum voltage of 5 V from the potentiometers to the 4.096 V of the voltage reference source. A Real-Time Clock (RTC) circuit was employed to timestamp the position data from the potentiometers. All data was written to an SD card in the data logger. The electric circuitry data logging device can be seen in the left side of Figure 28. The data logger was successfully used to record the time history of suspension displacement during a track day at *Sydney Motorsport Park*. However, due to limitations of SD card writing rate, and the Arduino Uno, a maximum sampling rate of between 30 to 40 Hz could be achieved. This presented an apparent aliasing issue in the data and a faster sampling rate was required. For example, the vibration data frequently showed 2-3 data points per period, which could not accurately represent the displacement vibrations. Due to the speed limitations of the Arduino, a commercial high-speed *Advantech USB-4704 Data Acquisition Module* was sourced instead (shown as the left device in Figure 29).

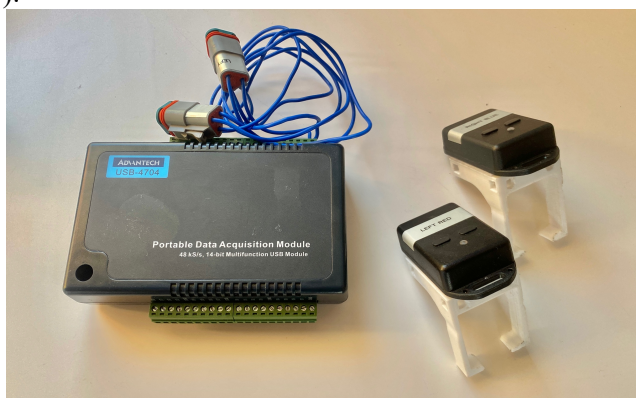

Figure 29: Advantech portable data acquisition module and IMU sensors stuck to 3D printed brackets for mounting to the wheel uprights.

Furthermore, three Inertial Measurement Unit (IMU) sensors were sourced to measure the vertical acceleration of the front wheels and chassis. Plastic brackets were designed, and 3D printed to hold the IMU sensors on the front wheels, as shown in Figure 29, and installed on the car in Figure 30 (right).

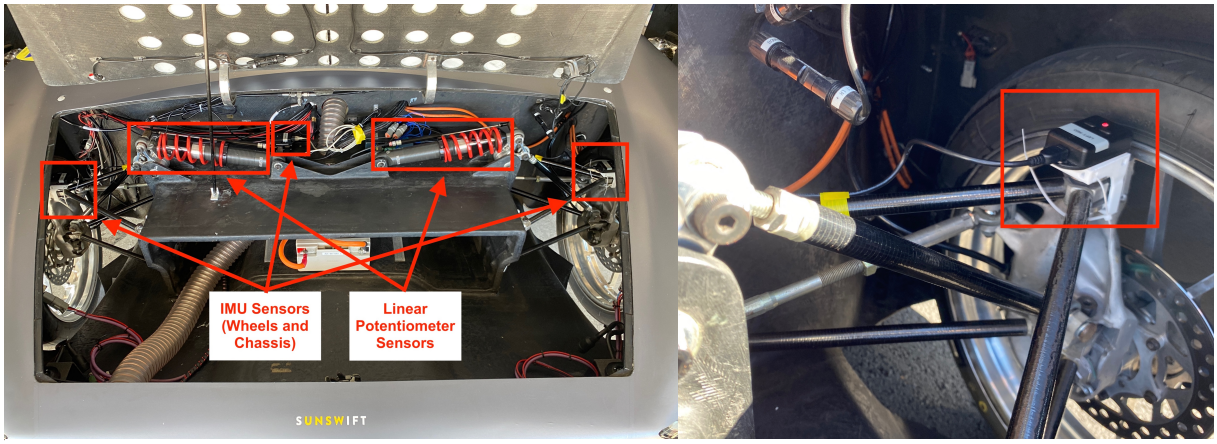

Figure 30: Sunswift VII Solar vehicle showing all sensors mounted to the front of the car (left) and a close-up of IMU sensor mounted to the left wheel.

The left side of Figure 30 shows all sensors installed on the vehicle. The data acquisition (DAQ) module is used to record the displacement data from the potentiometer sensors. The data is sent directly via USB cable to a computer in the vehicle. The IMU sensors could also be separately connected to the same computer directly via USB cable. To record the data from the DAQ module, a highspeed C++ program was written using functions supplied by the manufacturer as part of an Application Programming Interface (API). Similarly, a separate program was written to obtain data from the IMU sensors, using the API functions supplied by the manufacturer of the IMU. Both programs could be run simultaneously as separate programs. In each case, data entries were accurately time-stamped in milliseconds using a Unix timestamp which could be obtained using the *chrono* library in C++. The use of the Unix timestamp allowed both programs to remain synchronised, despite running as separate processes. Both C++ programs are shown in the Appendix.

8.2. Experimental Results

Unfortunately, the vehicle experienced powertrain problems during the day of testing and an experiment with the car powered could not be completed. However, the car could be pushed to the top of a long straight hill on the track at *Sydney Motorsport Park*. Figure 31 (right) shows the hill onto which the car was pushed, which corresponds to the position labelled *starting point* on the track map in Figure 31 (left).

Figure 31: The "Long Circuit" map at Sydney Motorsport Park (left), showing the region travelled during the experiment in red, and the corresponding view of the long straight section of the track and Sunswift VII car (right).

At the top of the hill, the car was loaded with four passengers and let roll in the direction indicated in in Figure 31. The displacement data from the potentiometers on front suspension, acceleration data from the IMU sensors, as well as vehicle velocity was then recorded as the vehicle rolled down the hill and came to a stop on the point marked *end point* on the map in Figure 31. The raw data is compiled in Figure 32.

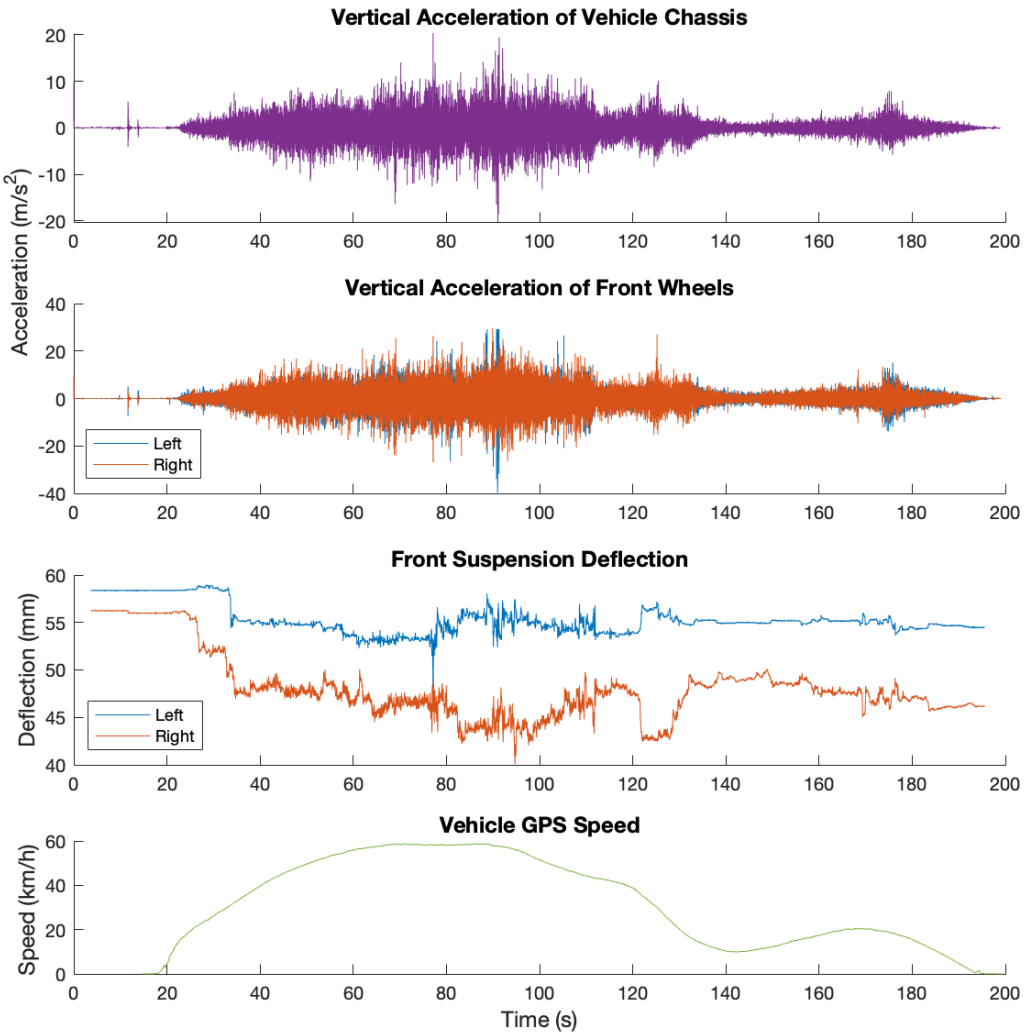

Figure 32: Raw sensor position (deflection), acceleration and speed data from the experiment.

The data shows that the vehicle accelerated to a maximum of 58 kmh^{-1} whilst rolling down the initial straight section of the track between the 50 to 100 second mark. During this time period the front suspension deflection time history clearly shows the disturbance induced by the road roughness. The suspension sag induced by the passengers entering the car can be seen around the 25 to 35 second mark. Additionally, the left suspension can be seen extending whilst the right suspension compresses near the 120 second mark as the vehicle chassis rolls due to the cornering forces induced in the left hand turn after the straight track section shown in Figure 31. The road roughness induced vibrations seen be the wheels and chassis are also clearly evident.

The time history data during which the vehicle reached its maximum velocity between the 50 to 100 second mark in Figure 32 was extracted and analysed separately, as shown in Figure 34. In addition, the suspension deflection velocity was found by numerically integration the displacement time data from the potentiometers in *Matlab*.

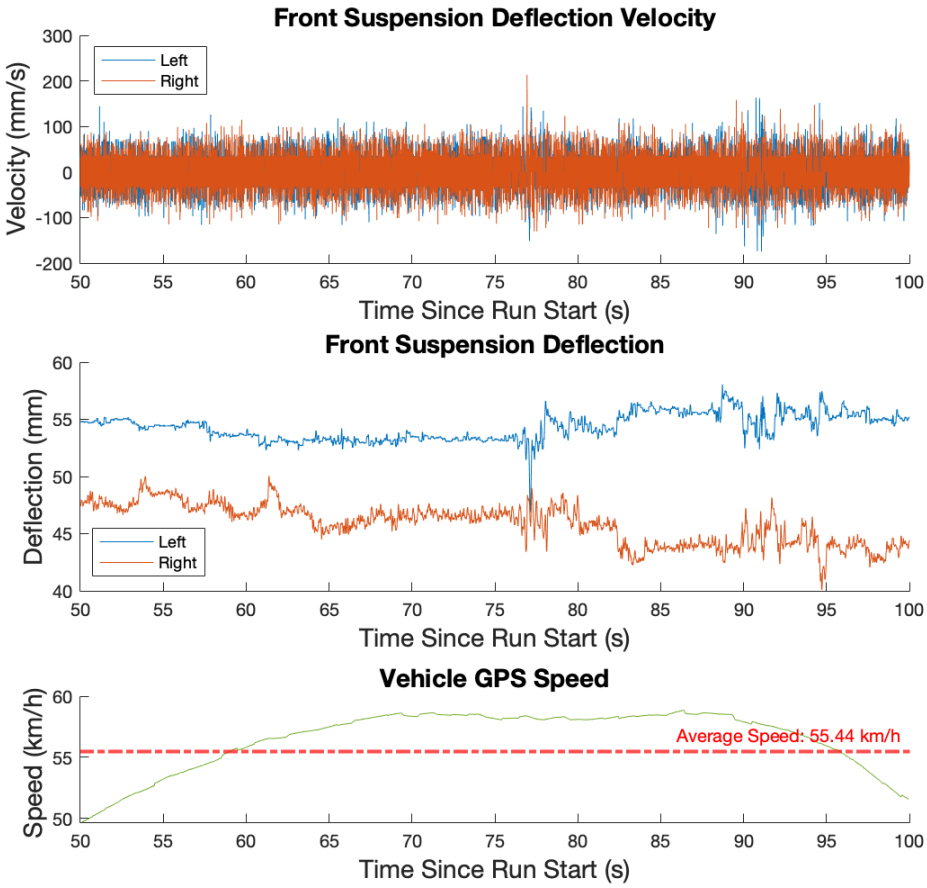

Figure 34: Front suspension deflection, deflection velocity and average vehicle velocity during 50 to 100 second mark.

The average velocity of the vehicle during the time interval is shown to be 55.44 kmh^{-1}. The front suspension deflection velocity time history is shown in the top of the figure. The power dissipation in the dampers is found by multiplying each velocity data point by the expected damping force generated at that velocity, as was done in section 5.4. As the damping force could not be directly measured, a *Matlab* script was written to calculate the expected damping force as a function of the deflection

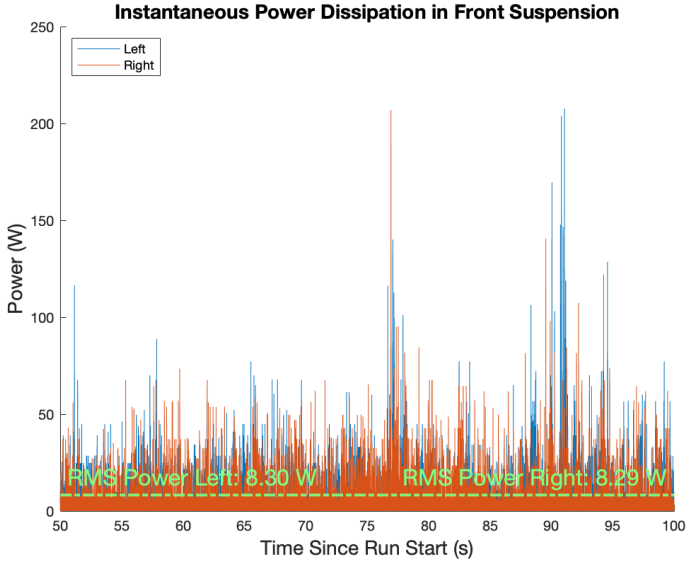

Figure 33:: Instantaneous and RMS power dissipation in the front dampers.

velocity based on the multilinear approximation of the damping behaviour found in section 4.4. The results in Figure 33 show the power dissipation time history and resulting RMS power dissipation in the dampers of approximately 8.3 W. This figure may seem low, but it can be expected considering the vehicle is travelling unpowered at a medium speed on a very smooth racetrack. Figure 35 shows the frequency histogram of the suspension deflection velocity and resulting damping force which is calculated as a function of the velocity.

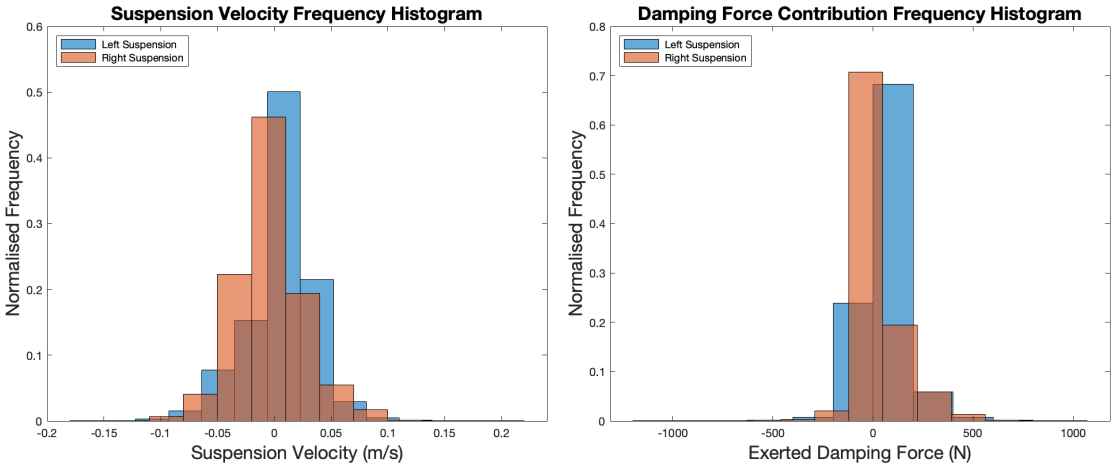

Figure 35: Suspension velocity frequency histogram, and corresponding exerted damping force frequency histogram of the front suspension during the 50 to 100 second mark of the experiment.

The front dampers do not exceed much further than $\pm$500 N of damping force, or $\pm$0.5 ms^{-1} damping velocity. Therefore, from the known damping characteristic of the front damper (Figure 16 in section 4.4), the damping velocity in this experiment was not strong enough for the damper to reach forces outside of the initial linear region.

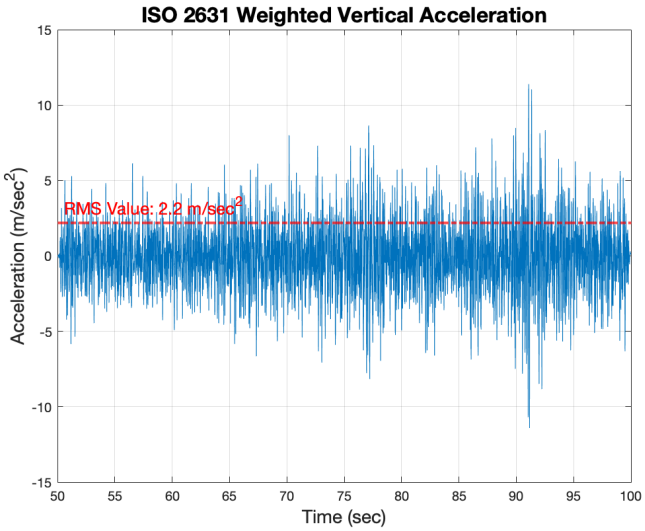

Figure 36: ISO 2631 frequency-weighted vertical chassis acceleration during the 50 to 100 second mark of the experiment.

The vertical chassis acceleration during the 50 to 100 second interval was also analysed. The RMS chassis acceleration was about 3.4 ms^{-2}. Using the *Vibrationdata Matlab Signal Analysis & Structural Dynamics Package* by Tom Irvine [67], the unfiltered vertical chassis acceleration could be numerically

frequency weighted using the ISO 2631 weightings W_k described in section 5.1. The resulting weighted acceleration time history in Figure 36 shows an RMS weighted acceleration value (a_{wz}) of 2.2 ms^{-2}. This value is very high when compared to the guidelines provided in the ISO 2631 standard (Table 7 in section 5.1), which would predict a *very uncomfortable* ride quality. This is likely because the Sunswift VII vehicle is very different to regular passenger vehicle for which the ISO 2631 standard is designed. The suspension dampers, spring stiffness and tyre stiffness are all much higher than regular passenger vehicles. Furthermore, the entire car features an incredibly stiff monocoque carbon fibre chassis construction which can be expected to attenuate vibration more than consumer grade cars. Although the ride comfort in the Sunswift car is noticeably poor as a passenger, further analysis is required to verify that the weighted acceleration value truly reflects the ISO 2631 standard. For example, Figure 37 shows the front wheel acceleration, chassis acceleration and suspension deflection for a split-second time segment, during which the car hit a cat-eye in the road with the left front wheel.

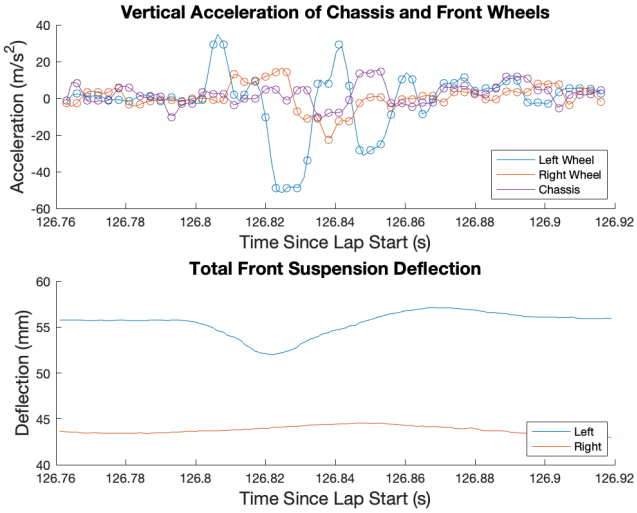

Figure 37: Vertical chassis acceleration, vertical front wheel acceleration and suspension deflection whilst hitting a small cat-eye bump with the left wheel at a speed of approx. 38 km.

The cat eye hits the front left wheel at approximately the 126.8 second mark, resulting in an initial upward acceleration of the left wheel, followed by violent high frequency vibrations in both wheels and the chassis. The downward acceleration spike of the left wheel after the 126.82 second mark reaches the maximum absolute acceleration threshold of the IMU sensor of 4G (which reads 5G in Figure 37 because the 1G mean acceleration due to gravity has been subtracted from the data shown in the figure). Following the impact, the left wheel, right wheel and chassis all vibrate with a very similar period, and the chassis and right wheel are approximately in phase, whereas the left wheel is approximately 180 degrees out of phase. Given that the suspension displacement data reveals dynamics that are much slower than the vibrations induced in the wheels and chassis, it can be theorised that chassis and wheels share complex natural vibration frequency modes which are not accounted for in the simulation dynamics.

8.3. Validation of Simulation Results

Due to the powertrain issues experienced by the *Sunswift VII* during the track day, the planned approach to validate the RMS power dissipation in the front dampers, as predicted by the Simulink simulation in section 7.1 was not possible. The planned validation method was to drive the vehicle on the same section of a straight road section (most likely the straight part of the racetrack which was analysed in section 8.2) whilst keeping the vehicle velocity constant. An approximately constant vehicle velocity can be achieved by using an on-board cruise control system, or manually by the driver's inputs. Next, the deflection time history for multiple increments of constant velocities on the same road section can then be recorded (like in Figure 34) and converted to instantaneous power in the damper (like in Figure 33). If the simulation revealed correct results, then plotting the RMS of power dissipated against the respective vehicle velocity, should produce a proportional relationship, provided that the road roughness is constant, as was shown in Figure 22 in section 7.1 of this report. Furthermore, the gradient of the relationship in the resultant graph should be related to the road roughness, as was determined section 7.1. An equivalent velocity-power graph to Figure 22 could then be generated in simulation which results in the same gradient. The road roughness coefficient of this simulation should correspond to the roughness coefficient of the real-world road segment. Given the simulation with input parameters (road gradient and velocity) which produce the same velocity-power relationship as the real-world data, quantities such as the Weighted RMS vertical ISO 2631 chassis acceleration, damper power generation and RMS vertical acceleration of the wheels could be compared between simulation and reality.

A less comprehensive validation approach was done using the data which was available. The vehicle velocity and u, was set to the average measured value during the experiment of 55.44 kmh^{-1} during the 50 to 100 second time period which was analysed in the previous section. In simulation, the road

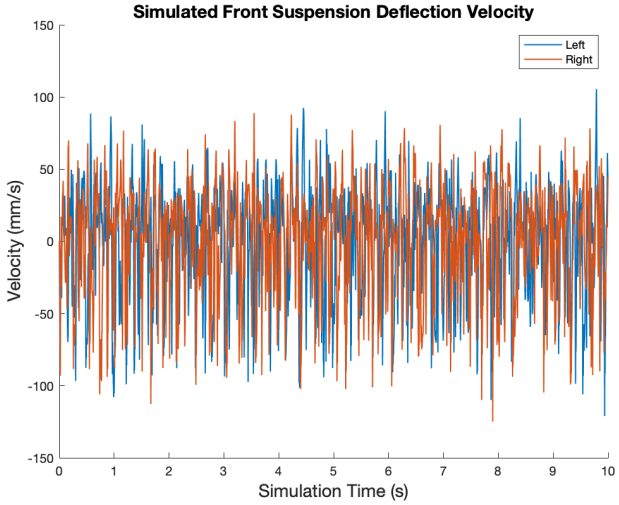

Figure 38: Simulated front suspension velocity under the same conditions as the experiment.

roughness coefficient $S_{PSD}(n_0)$, which resulted in the same average RMS suspension deflection velocity as the experimental data of (0.0301 ms^{-1}) was then found, as shown in Figure 38. This resulted in a road roughness coefficient $S_{PSD}(n_0)$ of 6.4 $(\times 10^{-6})$ m^3, which corresponds to a good quality ISO 8608 grade A road. This is realistic because the racecourse at Sydney Motorsport Park is very smooth and should be a very low roughness. Furthermore, the frequency histogram of the average front damping force in the simulation in Figure 38 shows that the damping force falls almost completely within the $\pm$500 N range which was also seen in the experimental data in Figure 35. The RMS power produced in the front dampers was the same as that in the experiment, which was calculated to be 8.3 W.

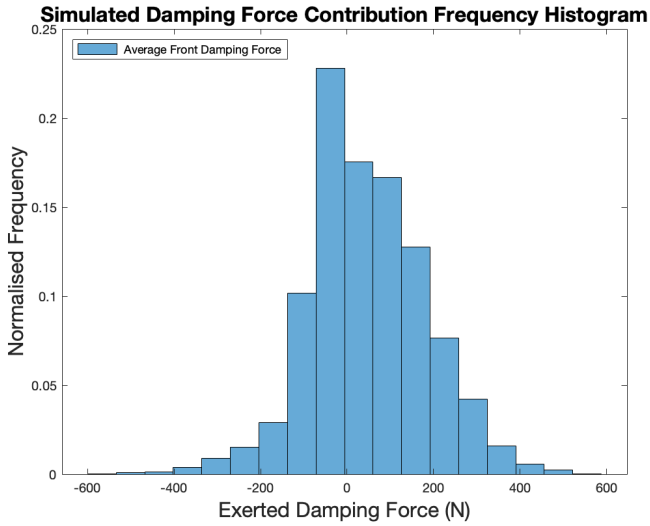

Figure 39: Simulated damping force frequency histogram.

9. Conclusion and Recommendation for Future Work

This report provides a critical evaluation of existing literature and commercial research involving Energy Harvesting Shock Absorbers for automotive applications. The existing designs could be categorised based on their principal of energy transduction. This included piezoelectric transducer-based and electromechanical transducer-based EHSAs. Electromechanical EHSA could be further categorised into direct drive and indirect drive electromechanical shock absorbers. Indirect drive prototypes showed durability and reliability issues, as a result of complex mechanical linkages and mechanisms. The current state-of-the art designs, such as a patent by Audi, and research prototypes employed planetary gearboxes in their designs. Such designs showed durability benefits arising from their simpler mechanical design and high torque transmitting ability of planetary gearboxes, as a result of superior gearing and efficient power transmission. The best designs showed impressive energy harvesting potential, with experimental prototypes of dampers reaching energy conversion efficiencies above 50% and a total efficiency above 30% when including the power electronic circuitry for storing electrical energy.

In this report, simulation studies were conducted to further explore the feasibility of EHSA, as applied to the *Sunswift VII Solar vehicle*. A comprehensive seven DOF full-car model was constructed to reflect the dynamics of the vehicle. Realistic road profiles could be generated based on the ISO 8608 standard. Furthermore, constraint criteria relating to the passenger comfort, road handling performance of the vehicle and physical suspension limitations were incorporated in the model. The simulation showed that the harvestable power in the vehicle suspension was proportional to the road roughness coefficient and vehicle velocity. With regards to the constraint criteria, a maximum attainable average power dissipation of 63.38 W per front damper and 60.56 W per rear damper was observed. Considering the efficiency of the state-of-the-art energy harvesting dampers which is around 30%, a realistic 18 W to 20 W of power could be harvested from the *Sunswift VII car*. Experimental road-tests showed that approximately 8.3 W was dissipated in each front dampers of the *Sunswift VII solar car* when travelling at 55 kmh^{-1} on a smooth racecourse. The experimental results showed similarity to the simulations, yet a comprehensive validation of simulations could not be done due to powertrain issues faced by the *Sunswift VII car* during track day. A dimensionless parameter sensitivity study showed that the average harvestable power in the vehicle suspension was very sensitive to the tyre stiffness, but relatively insensitive to the suspension properties. The mass of the wheels had little impact on the average harvestable power, whilst the chassis mass could be shown to improve the ride comfort and reduce the dynamic to static tyre force ratio at the wheels of the car, resulting in better road handling. The results of the parameter sensitivity analysis did generally agree with existing literature, including an analytical study which was based on a quarter car model. Some

discrepancies were observed between the simulation and this particular study which were attributed to the ability of the full car model to better approximate the real vehicle.

Some limitations of the simulative studies were already discussed in this report. The first step in improving the accuracy of the simulations should be to conduct a thorough validation study, such as the procedure described in section 8.3 of this report. Further improvements to the simulation could include a more accurate and realistic model of the vehicle tyres. The dynamic model of the vehicle assumes the tyres to be an ideal spring with linear stiffness, however real-life factors such as hysteresis are not considered. The tyre model should be a topic of particular focus, considering its effect on the power harvestable from the suspension. Furthermore, a frequency filter could be included in the road profile model to filter wavelengths shorter than the tyre patch. Some studies in literature also included the effect of friction forces in their simulations. The non-linear effects which result from the vehicle tyres losing ground contact could also be studied and added to the simulation.

This report showed that implementation of EHSA on the *Sunswift VII solar vehicle* could be worthwhile of pursuit. It is hoped that this report will inspire further research in this field and contribute to the development of more sustainable transportation solutions in the future.

10. Bibliography

1. Wang, X., *Frequency analysis of vibration energy harvesting systems*, ed. A. Press. 2016.
2. Magazine, G.B. *The Innovative Shock Absorber System From Audi: New Technology Saves Fuel And Enhances Comfort*. 2017; Available from: https://www.globalbrandsmagazine.com/the-innovative-shock-absorber-system-from-audi-new-technology-saves-fuel-and-enhances-comfort/.
3. (ISO), I.S.O., *ISO 8608 Mechanical vibration — Road surface profiles — Reporting of measured data*. 2016.
4. Liu, Y., L. Xu and L. Zuo, *Design, Modeling, Lab, and Field Tests of a Mechanical-Motion-Rectifier-Based Energy Harvester Using a Ball-Screw Mechanism.* IEEE/ASME Transactions on Mechatronics, 2017. **22**(5): p. 1933-1943.
5. Ebrahimi, B., et al., *A hybrid electromagnetic shock absorber for active vehicle suspension systems.* Vehicle System Dynamics, 2011. **49**(1-2): p. 311-332.
6. Zhao, Z., et al., *Energy Harvesting from Vehicle Suspension System by Piezoelectric Harvester.* Mathematical Problems in Engineering, 2019. **2019**: p. 1086983.
7. Yan, L., et al., *MAGNETIC FIELD OF TUBULAR LINEAR MACHINES WITH DUAL HALBACH ARRAY.* Progress In Electromagnetics Research, 2013. **136**: p. 283-299.
8. Galluzzi, R., et al., *Rotary regenerative shock absorbers for automotive suspensions.* Mechatronics, 2021. **77**: p. 102580.
9. Li, Z., et al., *Mechanical Motion Rectifier Based Energy-Harvesting Shock Absorber*. 2012. p. 595-604.
10. Knowles, D., *Automotive Suspension & Steering Systems*. Classroom Manual for Automotive Suspension & Steering Systems. 2007.
11. Gonzalez, A., et al., *An Innovative Energy Harvesting Shock Absorber System for Motorbikes.* IEEE/ASME Transactions on Mechatronics, 2021: p. 1-11.
12. Zhang, R., X. Wang and S. John, *A Comprehensive Review of the Techniques on Regenerative Shock Absorber Systems.* Energies, 2018. **11**(5): p. 1167.
13. Kong, L.B., et al., *Waste energy harvesting: Mechanical and thermal energies*. Vol. 24. 2014: Springer Science & Business Media.
14. Song, E.Y. and K. Lee, *Understanding IEEE 1451-Networked smart transducer interface standard-What is a smart transducer?* IEEE Instrumentation & Measurement Magazine, 2008. **11**(2): p. 11-17.
15. Priya, S., *Advances in energy harvesting using low profile piezoelectric transducers.* Journal of Electroceramics, 2007. **19**(1): p. 167-184.
16. Li, W.G., S. He and S. Yu, *Improving power density of a cantilever piezoelectric power harvester through a curved L-shaped proof mass.* IEEE Transactions On Industrial Electronics, 2009. **57**(3): p. 868-876.
17. Hendrowati, W., *Design, Modeling and Analysis of Implementing a Multilayer Piezoelectric Vibration Energy Harvesting Mechanism in the Vehicle Suspension.* Engineering, 2012. **04**: p. 728-738.
18. Xiao, H., X. Wang and S. John, *A dimensionless analysis of a 2DOF piezoelectric vibration energy harvester.* Mechanical Systems and Signal Processing, 2015. **58-59**: p. 355-375.

19. Tian, W., et al., *A Review of MEMS Scale Piezoelectric Energy Harvester.* Applied Sciences, 2018. **8**(4).
20. PD Mitcheson, E.R., PK Wright, EH Yeatman, *Transduction mechanisms and power density for MEMS inertial energy scavengers.* spiral.imperial.ac.uk, 2006.
21. Li, Z., et al., *Electromagnetic Energy-Harvesting Shock Absorbers: Design, Modeling, and Road Tests.* Vehicular Technology, IEEE Transactions on, 2013. **62**: p. 1065-1074.
22. T, J.E.M., *Brushless Permanent Magnet and Reluctance Motor Drives*. Monographs in Electrical and Electronic Engineering No.21, ed. R.L.G. P Hammond. 1989: Oxford Science Publications.
23. Tonoli, A. and N. Amati, *Dynamic Modeling and Experimental Validation of Eddy Current Dampers and Couplers.* Journal of Vibration and Acoustics, 2008. **130**.
24. Tonoli, A., *Dynamic characteristics of eddy current dampers and couplers.* Journal of Sound and Vibration, 2007. **301**(3): p. 576-591.
25. Zuo, L. and P.-S. Zhang, *Energy Harvesting, Ride Comfort, and Road Handling of Regenerative Vehicle Suspensions.* Journal of Vibration and Acoustics, 2013. **135**(1).
26. al, L.Z.e., *Design and characterization of an electromagnetic energy harvester for vehicle suspensions.* Smart Materials and Structures, 2019.
27. Wang, R., R. Ding and L. Chen, *Application of hybrid electromagnetic suspension in vibration energy regeneration and active control.* Journal of Vibration and Control, 2016. **24**(1): p. 223-233.
28. Austin Jughes, B.D., *Electric Motors and Drives*. 5 ed. 2015.
29. Karnopp, D., *Permanent Magnet Linear Motors Used as Variable Mechanical Dampers for Vehicle Suspensions.* Vehicle System Dynamics, 1989. **18**(4): p. 187-200.
30. Cheng, S. and D.P. Arnold, *A study of a multi-pole magnetic generator for low-frequency vibrational energy harvesting.* Journal of Micromechanics and Microengineering, 2009. **20**(2): p. 025015.
31. Choi, J. and J. Yoo, *Design of a Halbach Magnet Array Based on Optimization Techniques.* IEEE Transactions on Magnetics, 2008. **44**(10): p. 2361-2366.
32. Seok-Myeong, J., et al., *Comparison of three types of PM brushless machines for an electro-mechanical battery.* IEEE Transactions on Magnetics, 2000. **36**(5): p. 3540-3543.
33. ISO, *ISO 2631-1:1997 Mechanical vibration and shock — Evaluation of human exposure to whole-body vibration*, in *Part 1: General requirements*. 1997, International Organization for Standardization: URL: https://www.iso.org/standard/7612.html. p. 5-16.
34. Tang, X., T. Lin and L. Zuo, *Design and Optimization of a Tubular Linear Electromagnetic Vibration Energy Harvester.* IEEE/ASME Transactions on Mechatronics, 2014. **19**(2): p. 615-622.
35. Long, Z., G. He, and S. Xue, *Study of EDS & EMS Hybrid Suspension System With Permanent-Magnet Halbach Array.* IEEE transactions on magnetics, 2011. **47**(12): p. 4717-4724.
36. Park, M.S.a.J.Y., *Design and experiment of human hand motiondriven electromagnetic energy harvester usingdual Halbach magnet array.* Smart Materials and Structures, 2017.
37. Zhu, D., et al., *Increasing output power of electromagnetic vibration energy harvesters using improved Halbach arrays.* Sensors and Actuators A: Physical, 2013. **203**: p. 11-19.

38. Duong, M.-T., et al., *Optimal Design of a Novel Single-Phase 8-Slot 8-Pole Tubular Electromagnetic Shock Absorber to Harvest Energy.* IEEE Transactions on Industrial Electronics, 2020. **67**(2): p. 1180-1190.
39. Bastow, D., G. Howard and J.P. Whitehead, *Car suspension and handling*. 2004: SAE international Warrendale.
40. Yongchao, Z., et al. *Experimental verification of energy-regenerative feasibility for an automotive electrical suspension system*. IEEE.
41. al., S.e., *REGENERATIVE PASSIVE AND SEM-ACTIVE SUSPENSION*, U.S. Patent, Editor. 2006: USA.
42. al., S.e., *REGENERATIVE DAMPING METHOD AND APPARATUS*, U.S.P.A. Publication, Editor. 2004: USA.
43. Li, P. and L. Zuo, *Assessment of Vehicle Performances with Energy-Harvesting Shock Absorbers.* SAE International Journal of Passenger Cars - Mechanical Systems, 2013. **6**: p. 18-27.
44. Bowen, L., et al., *An Innovative Energy Harvesting Shock Absorber System Using Cable Transmission.* IEEE/ASME Transactions on Mechatronics, 2019. **24**(2): p. 689-699.
45. Audi Center, A.M. *Audi's latest chassis suspension system innovation: eROT (electromechanical rotary damper).* 2017; Available from: https://www.audi-mediacenter.com/en/press-releases/the-innovative-shock-absorber-system-from-audi-new-technology-saves-fuel-and-enhances-comfort-6551.
46. Audi AG, I.D., *ELECTROMECHANICAL DAMPER*, U.S.P.A. Publication, Editor. 2014.
47. Corsini, S., *Design of an electromechanical rotative damper prototype for automotive applications*. 2017 – 2018, POLITECNICO DI TORINO.
48. Cattabriga, G., *Design of a Speed Multiplier for regenerative Shock Absorber*, in *Dipartimento di Ingegneria Meccanica e Aerospaziale*. 2017 - 2018, Politecnico di Torino.
49. Tenerelli, R.A., *ENERGY MANAGEMENT TECHNIQUES FOR REGENERATIVE ACTIVE SHOCK ABSORBERS*, in *Degree Course in Mechatronic Engineering*. 2018: Politechnico di Torino.
50. Liu, H., H. Gao, and P. Li, *Handbook of vehicle suspension control systems*. 2013: Institution of Engineering and Technology.
51. Maher, D. and P. Young, *An insight into linear quarter car model accuracy.* Vehicle system dynamics, 2011. **49**(3): p. 463-480.
52. Knowlan, D., *Chassis Sim: The Damper Workbook*. 2021, Chassis Sim Technologies.
53. Riley, W. and A. George, *2002-01-3300 Design, Analysis and Testing of a Formula SAE Car Chassis.* 2002.
54. Chen, W., et al., *Integrated vehicle dynamics and control*. 2016: John Wiley & Sons.
55. Goenaga, B., L.G.F. Pumarejo, and O.A.M. Lerma, *Evaluation of the methodologies used to generate random pavement profiles based on the power spectral density: An approach based on the International Roughness Index.* Revista Ingenieria E Investigacion, 2017. **37**: p. 49-57.
56. Adrian Jensen, P., S.S.M.E.K. Hamilton, and S.M. Engineer. *PSD Random Vibration Analysis in FEMAP - An Introduction to the Hows and Whys of PSD*. in *Siemens Applied CAx*. 2017.
57. Múčka, P., *Simulated Road Profiles According to ISO 8608 in Vibration Analysis.* Journal of Testing and Evaluation, 2018. **46**: p. 20160265.

58. Austroads. *About Austroads*. 2023; Available from: https://austroads.com.au/about-austroads.
59. Pawar, P.R., A.T. Mathew and M.R. Saraf, *IRI (International Roughness Index): An Indicator Of Vehicle Response.* Materials Today: Proceedings, 2018. **5**(5, Part 2): p. 11738-11750.
60. Vyas, V.D.R.J.S., *Modelling of Automotive Suspension Damper*, in *School of Engineering Sciences* 2020, KTH Royal Institute of Technology KTH Royal Institute of Technology
61. Loprencipe, G. and P. Zoccali, *Ride Quality Due to Road Surface Irregularities: Comparison of Different Methods Applied on a Set of Real Road Profiles.* Coatings, 2017. **7**(5): p. 59.
62. Zuo, L. and S. Nayfeh, *Low order continuous-time filters for approximation of the ISO 2631-1 human vibration sensitivity weightings.* Journal of Sound and Vibration, 2003. **265**: p. 459-465.
63. Müller, P., K. Popp and W. Schiehlen, *Covariance Analysis of Nonlinear Stochastic Guide Way-Yehicle-Systems*, in *The Dynamics of Vehicles on roads and on tracks*. 2018, Routledge. p. 337-351.
64. Zuo, L. and S.A. Nayfeh, *Structured H2 Optimization of Vehicle Suspensions Based on Multi-Wheel Models.* Vehicle System Dynamics, 2003. **40**(5): p. 351-371.
65. Cantisani, G., et al., *Methods for Measuring and Assessing Irregularities of Stone Pavements—Part II.* Sustainability, 2023. **15**(4): p. 3715.
66. Cantisani, G. and G. Loprencipe, *Road Roughness and Whole Body Vibration: Evaluation Tools and Comfort Limits.* Journal of Transportation Engineering, 2010. **136**(9): p. 818-826.
67. Irvine, T. *Vibrationdata Matlab Signal Analysis & Structural Dynamics Package*. Available from: https://vibrationdata.wordpress.com/.

Appendix A – Vehicle Dynamics Differential Equations

Dynamic equations for motion of the wheels (un-sprung masses) $M_{FL}, M_{FR}, M_{RL}, M_{RR}$:

$$M_{FL}\ddot{z_{FL}} = K_T(z_{GFL} - z_{FL}) + K_{FL}(z_{BFL} - z_{FL}) + C_{FL}(\dot{z_{BFL}} - \dot{z_{FL}})$$
$$M_{FR}\ddot{z_{FR}} = K_T(z_{GFR} - z_{FR}) + K_{FR}(z_{BFR} - z_{FR}) + C_{FR}(\dot{z_{BFR}} - \dot{z_{FR}})$$
$$M_{RL}\ddot{z_{RL}} = K_T(z_{GRL} - z_{RL}) + K_{RL}(z_{BRL} - z_{RL}) + C_{RL}(\dot{z_{BRL}} - \dot{z_{RL}})$$
$$M_{RR}\ddot{z_{RR}} = K_T(z_{GRR} - z_{RR}) + K_{RR}(z_{BRR} - z_{RR}) + C_{RR}(\dot{z_{BRR}} - \dot{z_{RR}})$$

Dynamic equation for car body (sprung mass) M_B, pitch I_B and roll I_R:

$$M_B\ddot{z_B} = K_{FL}(z_{FL} - z_{BFL}) + C_{FL}(\dot{z_{FL}} - \dot{z_{BFL}}) + K_{FR}(z_{FR} - z_{BFR}) + C_{FR}(\dot{z_{FR}} - \dot{z_{BFR}})$$
$$+ K_{RL}(z_{RL} - z_{BRL}) + C_{RL}(\dot{z_{RL}} - \dot{z_{BRL}}) + K_{RR}(z_{RR} - z_{BRR}) + C_{RR}(\dot{z_{RR}} - \dot{z_{BRR}})$$

$$I_B\ddot{\theta}_B = -L_F K_{FL}(z_{FL} - z_{BFL}) - L_F C_{FL}(\dot{z_{FL}} - \dot{z_{BFL}}) - L_F K_{FR}(z_{FR} - z_{BFR})$$
$$- L_F C_{FR}(\dot{z_{FR}} - \dot{z_{BFR}}) + L_B K_{RL}(z_{RL} - z_{BRL}) + L_B C_{RL}(\dot{z_{RL}} - \dot{z_{BRL}})$$
$$+ L_B K_{RR}(z_{RR} - z_{BRR}) + L_B C_{RR}(\dot{z_{RR}} - \dot{z_{BRR}})$$

$$I_R\ddot{\varphi}_B = L_L K_{FL}(z_{FL} - z_{BFL}) + L_L C_{FL}(\dot{z_{FL}} - \dot{z_{BFL}}) - L_R K_{FR}(z_{FR} - z_{BFR})$$
$$- L_R C_{FR}(\dot{z_{FR}} - \dot{z_{BFR}}) + L_L K_{RL}(z_{RL} - z_{BRL}) + L_L C_{RL}(\dot{z_{RL}} - \dot{z_{BRL}})$$
$$- L_R K_{RR}(z_{RR} - z_{BRR}) - L_R C_{RR}(\dot{z_{RR}} - \dot{z_{BRR}})$$

The displacement at each corner of the body of the car, z_{BXX}, is given by the displacement of its mass centre z_B, plus the angular contribution from the vehicle pitch θ and roll φ, which for small angles is given by:

$$z_{BFL} = z_B - L_F \cdot \sin(\theta) + L_L \cdot \sin(\varphi) \approx z_B - L_F \cdot \theta + L_L \cdot \varphi$$
$$z_{BFR} = z_B - L_F \cdot \sin(\theta) - L_R \cdot \sin(\varphi) \approx z_B - L_F \cdot \theta - L_R \cdot \varphi$$
$$z_{BRL} = z_B + L_B \cdot \sin(\theta) + L_L \cdot \sin(\varphi) \approx z_B + L_B \cdot \theta + L_L \cdot \varphi$$
$$z_{BFL} = z_B + L_B \cdot \sin(\theta) - L_R \cdot \sin(\varphi) \approx z_B + L_B \cdot \theta - L_R \cdot \varphi.$$

The remaining variables are illustrated on the seven DOF car model in Figure 10 and their values are given in Table 1.

Appendix B – Compiled Austroads Road Deterioration Survey Data

Test Site ID	Location of Test Site		Surface Type	International Roughness Index (IRI)	Road Surface Power Spectrum (Angular Spatial Frequency Units) - ISO	Road Surface Power Spectrum (Spatial Frequency Units) - ISO	Road Classification (ISO8608)	Test Site Survey Date
	State	Road						
QL02	QLD	Bruce Highway, Beerburrum	Asphalt/CR base/gravel	0.99	0.20	3.21	A	27/2/18
QL04	QLD	Warrego Highway, Ipswich	Asphalt/CR base/CTCR	1.32	0.36	5.71	A	15/3/18
ARRB1	QLD	Rainbow Beach Road, Rainbow Beach	Spray seal/bound granular	3.52	2.54	40.59	B	3/3/18
NS03	NSW	Federal Highway, Collector	JPCP/lean mix concrete	1.82	0.68	10.85	A	31/1/18
NS17	NSW	Foreshore Road, Botany	CRCP	1.90	0.74	11.83	A	15/12/17
NS20	NSW	Pacific Motorway, Somersby	Asphalt/macadam	1.05	0.23	3.61	A	30/1/18
NS24	NSW	Pacific Highway, Tomago	Crushed basalt/GS/HL	0.83	0.14	2.26	A	30/1/18
NS25	NSW	Pacific Highway, Tomago	Crushed basalt/GS/HL	1.44	0.42	6.79	A	30/1/18
ARRB2	NSW	Monaro Highway, Cooma	Spray seal/bound granular	1.72	0.61	9.69	A	31/1/18
SA06	SA	Port River Express, Port Adelaide	Asphalt/CTCR	1.66	0.56	9.03	A	16/12/17
SA07	SA	Dukes Highway, Cooke Plains	Spray seal/unbound granular	1.37	0.38	6.15	A	16/12/17
VC20	VIC	Hume Highway, Benalla	Seal/unbound CR	2.37	1.15	18.40	A	15/12/17
VCA04	VIC	Eastern Freeway, Donvale	Asphalt/CTCR	1.11	0.25	4.04	A	22/1/18
ACT01-P1	ACT	Uriarra Road, Stromlo	Spray Seal/UBCR	2.56	1.34	21.47	A	9/10/17
ACT01-C1	ACT	Uriarra Road, Stromlo	Spray Seal/UBCR	2.36	1.14	18.25	A	9/10/17
ACT02-C2	ACT	Drakeford Drive, Kambah	Asphalt/UBCR	2.67	1.46	23.35	A	9/10/17
ACT02-C3	ACT	Drakeford Drive, Kambah	Asphalt/UBCR	2.97	1.81	28.90	A	9/10/17
ACT03-C1	ACT	Isabella Drive, Macarthur	Asphalt/UBCR	1.89	0.73	11.70	A	10/10/17
ACT03-C2	ACT	Isabella Drive, Macarthur	Asphalt/UBCR	1.81	0.67	10.73	A	10/10/17
ACT04-P1	ACT	Yamba Drive, Isaacs	Asphalt/UBCR	2.37	1.15	18.40	A	9/10/17
ACT04-P2	ACT	Yamba Drive, Isaacs	Asphalt/UBCR	2.34	1.12	17.94	A	9/10/17
ACT05-C1	ACT	Yarra Glen, Curtin	Deep Strength/UBCR	2.40	1.18	18.87	A	9/10/17
ACT05-C2	ACT	Yarra Glen, Curtin	Deep Strength/UBCR	2.21	1.00	16.00	A	9/10/17
ACT06-P1	ACT	Monaro Highway, Fyshwick	Deep Strength/UBCR	1.91	0.75	11.95	A	9/10/17
ACT06-P2	ACT	Monaro Highway, Fyshwick	Deep Strength/UBCR	2.03	0.84	13.50	A	9/10/17
LTPPM1-S1	VIC	Stud Road, Dandenong North	Asphalt/unbound granular	2.27	1.06	16.88	A	22/1/18
LTPPM1-S2	VIC	Stud Road, Dandenong North	Asphalt/unbound granular	3.15	2.03	32.51	B	22/1/18
LTPPM1-S3	VIC	Stud Road, Dandenong North	Asphalt/unbound granular	2.38	1.16	18.56	A	22/1/18
LTPPM1-S4	VIC	Stud Road, Dandenong North	Asphalt/unbound granular	2.47	1.25	19.99	A	22/1/18
LTPPM1-S5	VIC	Stud Road, Dandenong North	Asphalt/unbound granular	1.80	0.66	10.61	A	22/1/18
LTPPM2-S1	VIC	Western Highway, Gerang Gerung	Spray seal/unbound granular	3.61	2.67	42.69	B	23/4/18
LTPPM2-S2	VIC	Western Highway, Gerang Gerung	Spray seal/unbound granular	2.46	1.24	19.82	A	23/4/18
LTPPM2-S3	VIC	Western Highway, Gerang Gerung	Spray seal/unbound granular	2.18	0.97	15.57	A	23/4/18
LTPPM2-S4	VIC	Western Highway, Gerang Gerung	Spray seal/unbound granular	2.71	1.50	24.06	A	23/4/18
LTPPM2-S5	VIC	Western Highway, Gerang Gerung	Spray seal/unbound granular	2.65	1.44	23.01	A	23/4/18
LTTPM4-S1	VIC	South Gippsland Highway, Woodside	Spray seal/unbound granular	3.01	1.86	29.68	A	1/5/18
LTTPM4-S2	VIC	South Gippsland Highway, Woodside	Spray seal/unbound granular	3.06	1.92	30.67	A	1/5/18
LTTPM4-S3	VIC	South Gippsland Highway, Woodside	Spray seal/unbound granular	3.46	2.45	39.22	B	1/5/18
LTTPM4-S4	VIC	South Gippsland Highway, Woodside	Spray seal/unbound granular	5.55	6.31	100.91	B	1/5/18
LTTPM4-S5	VIC	South Gippsland Highway, Woodside	Spray seal/unbound granular	4.88	4.88	78.01	B	1/5/18
LTPPM5-S1	QLD	Bruce Highway, North of Ingham	Spray seal/unbound granular	1.88	0.72	11.58	A	12/5/18
LTPPM5-S2	QLD	Bruce Highway, North of Ingham	Spray seal/unbound granular	3.03	1.88	30.08	A	12/5/18
LTPPM5-S3	QLD	Bruce Highway, North of Ingham	Spray seal/unbound granular	2.37	1.15	18.40	A	12/5/18
LTPPM5-S4	QLD	Bruce Highway, North of Ingham	Spray seal/unbound granular	2.90	1.72	27.55	A	12/5/18
LTPPM5-S5	QLD	Bruce Highway, North of Ingham	Spray seal/unbound granular	2.39	1.17	18.71	A	12/5/18
LTPPM7-S1	NSW	Great Western Highway, Blacktown	Asphalt/unbound granular	1.20	0.29	4.72	A	4/5/18
LTPPM7-S2	NSW	Great Western Highway, Blacktown	Asphalt/unbound granular	1.60	0.52	8.39	A	4/5/18
LTPPM7-S3	NSW	Great Western Highway, Blacktown	Asphalt/unbound granular	1.25	0.32	5.12	A	4/5/18
LTPPM7-S4	NSW	Great Western Highway, Blacktown	Asphalt/unbound granular	1.12	0.26	4.11	A	4/5/18
LTPPM7-S5	NSW	Great Western Highway, Blacktown	Asphalt/unbound granular	1.34	0.37	5.88	A	4/5/18

* AC: asphalt; SS: sprayed seal; DS: deep strength; LM: lean mix; CR: crushed rock; UB: unbound; BEC: bitumen emulsion cement; B: bound; M: macadam; JPCP: jointed plain reinforced concrete pavement; CR: crushed rock; CRCP: continuously reinforced concrete pavement; CTCR: cement-treated crushed rock; GS: granulated slag; HL: Hydrated Lime.